DOE/ET-53088-227

IFSR #227

# Simulation Study of Two-Ion Hybrid Resonance Heating

*S. Riyopoulos* and *T. Tajima*

Institute for Fusion Studies
The University of Texas at Austin
Austin, Texas 78712-1060

February 1986

# Simulation Study of Two-Ion Hybrid Resonance Heating

*S. Riyopoulos* and *T. Tajima*
Institute for Fusion Studies
The University of Texas at Austin
Austin, Texas 78712-1060

## Abstract

A one-dimensional low-noise, low-frequency electromagnetic particle simulation code that is appropriate for investigation of ion cyclotron resonance heating (ICRH) is developed. Retaining the hyperbolicity of the electromagnetic waves and exploiting nearly one-dimensional characteristics (perpendicular to the external magnetic field) of the ICRH, the guiding center electron approximation for the transverse electronic current calculation is used. Mode conversion of the incoming magnetosonic wave into the electrostatic ion–ion hybrid mode is observed accompanied by strong ion-heating. The dependence of this heating on the different plasma parameters is examined through a series of simulations, focusing mainly on wave incidence from the high field side. Because $k_{\|} = 0$ in the runs, the conventional Landau damping cannot explain the ion heating. Non-linear mechanisms for energy transfer are discussed. The numerical results demonstrate the importance of the non-linear wave particle interaction for energy absorption during radio frequency heating in the ion cyclotron regime.

## I. Introduction

The ion cyclotron resonance heating (ICRH) has been regarded as one of important heating methods of magnetized plasmas as capable of directly heating ions. Heating of a plasma with two (or more) species of ions has attracted particular attention for fusion applications.[1] In this heating method, a propagating fast magnetosonic wave in the ion cyclotron frequency regime is applied on a magnetized plasma with two-ion species and usually the heavier ion as majority. When the magnetosonic wave is launched from the side of the weak magnetic field, it encounters the minority cyclotron resonance before the ion–ion hybrid resonance heating the minority ions.[1] When the magnetosonic wave is launched from the high magnetic field side, the ion–ion hybrid resonance is met before the minority ion cyclotron. In the cold plasma theory, the wave must be tunneled to the cyclotron resonance layer; with the inclusion of the finite Larmor radius effects, the wave is mainly mode-converted to a short wavelength electrostatic wave,[2–6] eventually dumping its energy into the plasma. For the alternative case with the lighter of the ions as majority, the above sequence of resonances is reversed.

Experimental results[7–8] with the antenna placed on the high field side have shown that localized ion heating takes place closer to the hybrid than the minority cyclotron layer and that this heating persists even when the cyclotron layer is placed outside the plasma. The energy transfer to the ions cannot be attributed to conventional Landau damping in view of negligible $k_{||}$ and the fact that the difference between the ion hybrid frequency $\omega_{IH}$ and the minority cyclotron frequency $\Omega_\beta$ is typically of order $\frac{1}{10}\Omega_\beta$ for minority concentration 10–20%. Non-linear wave particle interaction, stochastic as well as coherent, can be the heating mechanism. It is necessary to delineate this situation for analysis. Numerical calculations on ion–ion hybrid heating have been carried out by integration of the differential equation for wave propagation in inhomogeneous medium. The energy absorption has been provided by the linear theory Landau damping coefficient. So far, however, no computation using a particle code plasma model has appeared on the ICRH time scale without excessive electron noise. Inclusion of self-consistent ion dynamics is indispensable in opening all the channels for energy absorption including non-linear particle trapping and turbulent diffusion caused by the stirring of fluctuations. For this purpose, we construct a physical

model for computation and carry out the particle simulation based on the model.

The standard electromagnetic particle code[9,10] retaining full electron dynamics has been successfully used to describe wave propagation in the high-frequency regime, as for example the study of the upper hybrid wave propagation and mode conversion by Lin et al.[11] However, inclusion of the full electron dynamics makes the code too costly and too noisy to run on the ion cyclotron period time scales. Numerical stability considerations limit the simulation time step to the electron characteristic periods, much shorter than the relevant time scales for the ion motion. The need to suppress the noise levels also arises during low-frequency, small phase velocity runs as the typical electric fields of the launched waves are smaller than that in case of high-frequency, large phase velocity waves. This is seen from the scaling $E/B_0 = (v_{ph}/c)\,(B/B_0)$ given that $B/B_0$ is limited to a few percent for linearity and that $v_{ph}/c \sim v_A/c < 10^{-1}$ for usual tokamak parameters. It is beneficial to reduce the unnecessary electron noise in the simulation while keeping the full ion dynamics.

Therefore, there has been a considerable motivation in recent years for generating numerical algorithms suppressing the electron dynamics to the minimum required, depending on the situation under consideration. One approach is to utilize a simplified model with the exact electron motion reduced by time-averaging to the guiding center motion while keeping the full ion dynamics, as described by the drift-kinetic equations. A second approach may be to treat electrons as a massless cold neutralizing dielectric fluid while ions are treated as particles. Thus, fluid-particle "hybrid" codes have been developed. Electrostatic hybrid codes have been developed by Okuda et al.[12,13] in which electrons are treated as a fluid producing a dielectric shielding for ions in Poisson's equation. The applicability of the electrostatic model is limited to one-dimensional cases and for short wavelength low phase velocity waves, such as ion Bernstein modes near cyclotron harmonics.

In the general case of wave propagation across a magnetized plasma, such as a fast magnetosonic mode, both the electrostatic and the electromagnetic field components, coupled through the external $B$-field, must be retained. The need to include the electron response to the transverse electric field makes the electrostatic shielding method hardly adequate even in one dimension. Full treatment of the fields is especially important dur-

ing mode conversion in order to simulate the progressive change in the wave character, from mainly electrostatic to mainly transverse and vice versa. Electromagnetic hybrid codes such as the ones developed by Byers et al.[14] and Hewett et al.[15] have evolved from the magnetoinductive model with full particle dynamics for both electrons and ions.[16,17] Common characteristic in the above algorithms is that they employ the quasineutrality assumption $n_e \approx n_i = n_o$ and the resulting generalized Ohm's law in order to compute the electron charge and current density source terms from the ion charge and current density. The displacement current is omitted from Maxwell's equations, justified for $v_{\text{phase}} \ll c$, and the wave equation for the transverse electromagnetic components becomes an elliptic equation (magnetoinductive model).

We adopt the first approach following the electron guiding center motion[18] in the direction perpendicular to the external magnetic field and retaining the full set of Maxwell's equations. For the electron motion parallel to the magnetic field, the electrostatic screening method[12] may be extended to include the effects of small but finite $k_{||}$ without increasing the dimensionality of the code. The present model is generally applicable to problems of electromagnetic wave propagation in a strongly magnetized plasma with a wave frequency much below the electron cyclotron frequency. A model following drifting electrons coupled with the magnetoinductive field solver has been developed by Cheng et al.[19] and by Geary et al.[20]

Our goal in this paper is dual: First we implement such an algorithm that retains the hyperbolicity of the electromagnetic field equation for wave propagation in one dimension. Second we employ this code in order to simulate the mode conversion and particle heating taking place as a fast magnetosonic mode propagates towards the ion–ion hybrid layer in a two-ion species plasma. Summarizing the results, strong energy deposition and plasma heating with $k_{||} = 0$ has been observed. Energy absorption occurs for both minority and majority ions during incidence from the high field side, connected with an almost complete mode conversion from magnetosonic to electrostatic mode. The heating rate depends on the plasma parameters, but in fact is not very different for both ion species. A selective minority heating is observed during incidence from the low field side while an almost total reflection of the incoming magnetosonic mode off the ion hybrid layer is observed. High

minority temperatures are achievable; however, the overall energy absorption appears to be less than in the case of high field side because of the limited response by the majority ions.

The rest of the paper is organized as follows. The numerical algorithm is discussed in Section II. The plasma model and the boundary conditions are described in the same section. In Section III we present a review of the theory on ion–ion hybrid mode conversion and the associated heating mechanisms. The results of our numerical simulations are presented in Section IV and they are discussed in connection with the theory.

## II. Description of the Low-Frequency Low-Noise Code for Wave Heating

### *A. Numerical algorithm*

We wish to correctly describe the collective behavior of a plasma with two-ion species in a magnetic field. The full set of Maxwell's equations including the displacement current is retained. The time centered discretized form of the wave equations for the transverse field components is

$$E^n = E^{n-1} + c\Delta t \left\{ (\nabla \times B)^{n-1/2} - \frac{4\pi}{c} j^{n-1/2} \right\} \tag{1a}$$

$$B^{n+1/2} = B^{n-1/2} - c\Delta t (\nabla \times E)^n \tag{1b}$$

while the electrostatic component for the electric field is found from Poisson's equation

$$\nabla \cdot E^n = -4\pi\rho^n, \tag{2}$$

where the superscripts refer to the time step.

The field components are advanced in Fourier space and transformed back to real space for particle pushing. We focus on wave propagation in the $x$ direction, perpendicular to the magnetic field taken along the $z$ axis (Fig. 1). In such a case the ordinary electromagnetic mode with electric polarization parallel to the magnetic field $(0, 0, E_z)$ becomes decoupled from the extraordinary (fast magnetosonic) mode and propagates independently across the magnetic field with the speed of light $c$, while the magnetosonic propagates near the Alfvén speed $v_A = \left(B^2/4\pi\rho_0\right)^{1/2}$ where $\rho_0$ is the mass density. That limits the number of wave

components under examination to $\underline{E} = (E_x, E_y, 0)$, $\underline{B} = (0, 0, B_z)$. As a consequence, there is no force driving the particles along the $z$ direction and only two velocity components are required to compute the particle response $\underline{v} = (v_x, v_y)$.

The current and charge density source terms on the right-hand side of Eqs. (1) and (2) are computed from the particle positions and velocities

$$j_I^{n-1/2} = \sum_i v_i^{n-1/2} S\left(x_i^{n-1/2} - X_I\right) \tag{3}$$

$$\rho_I^n = \sum_i q_i S\left(x_i^n - X_I\right) \tag{4}$$

where the superscript denotes the time step, $x_i, v_i$ are the $i$th particle position and velocity respectively, $I$ in $X_I$ signifies the $I$th grid position, and $S$ is a form factor arranging the distribution of particle charge to nearby grid points.

The set of Eqs. (1)–(4) is closed by the dynamic equations of motion advancing particle position and velocity in time. For ions, the numerical version of the exact equations of motion is used

$$\begin{aligned} \underline{v}_i^{n-1/2} &= \underline{v}_i^{n-3/2} + \Delta t \underline{F}\left\{\underline{E}^{n-1}\left(x_i\right), \underline{B}^{n-1}\left(x_i\right)\right\} \\ x_i^n &= x_i^{n-1} + \Delta t v_i^{n-1/2} \end{aligned} \tag{5}$$

where $\underline{F}$ symbolizes the appropriate time centered scheme for the force $\underline{F} = e[\underline{E} + (\underline{v} \times \underline{B})/c]$ discussed elsewhere, $E\left(x_i\right)$ $(B(x_i))$ is the interpolated value for the electric (magnetic) field in the particle position between grid points and $B^{n-1} = 1/2\{B^{n-1/2} + B^{n-3/2}\}$. So far, the time centering of Eqs. (1)–(5) yields $\underline{E}$, $x$ and $\rho$ at integer time steps while $\underline{B}$, $\underline{v}$ and $\underline{j}$ are computed at half-time steps.

Electrons are advanced using the lowest order guiding center motion, the drift equation

$$v^{n+1/2} = \frac{1}{c}\left[E^{n+1/2}\left(x_i\right) \times B^{n+1/2}\left(x_i\right)\right] \tag{6}$$

and ignoring $\nabla B$ and curvature drifts (which, however, can be trivially included). Compared to the full cold plasma dielectric response tensor, our approach retains the cold electron contribution to the off-diagonal elements

$$\epsilon_{xy} = -\epsilon_{yx} = -i \sum_\sigma \frac{\Omega_\sigma}{\omega} \frac{\omega_\sigma^2}{\omega^2 - \Omega_\sigma^2}, \tag{7}$$

while it neglects the electron polarization current (coming from the electron acceleration parallel to the electric field) that contributes into the diagonal part of the dielectric tensor

$$\epsilon_{xx} = \epsilon_{yy} = 1 - \sum_{\sigma} \frac{\omega_\sigma^2}{\omega^2 - \Omega_\sigma^2}, \tag{8}$$

where $\omega_\sigma$ and $\Omega_\sigma$ are the plasma frequency and the cyclotron frequency associated with species $\sigma$. By inspection of Eq. (7) we see that the electron drift contribution is of the same order as the ion drift and must be kept, while according to Eq. (8), the electron polarization term scales as $\left(\omega_e/\Omega_e\right)^2 \Big/ \left(\omega_i/\Omega_i\right)^2 = m_e/m_i$ compared to the ion polarization term and can indeed be neglected at the limit $m_e/m_i \to 0$.

Equation (6) does not allow any energy exchange between the fields and the electrons, thus excludes electron Landau damping. This is of no great importance in case $k_{||} \cong 0$ and when the intended purpose is the selected energy deposition into the ions. For finite $k_{||}$, an extended version of the code including all three field and velocity components is appropriate with the electron motion split into two parts: the perpendicular to the magnetic field expressed by the drift Eq. (6), and the parallel to the magnetic field treated with the exact equation $dv_z/dt = (e/m)E_z$.

However, in case of small $k_{||}$ and with the electron Landau damping neglected we can still avoid following the exact parallel electron dynamics and retain the one-dimensional modeling. The electron-shielding effect due to the parallel motion to the magnetic field can be incorporated, using the electron dielectric response into Poisson's equation

$$i\underline{k} \cdot \underline{E}(\underline{k}) = -4\pi \left[\rho_i(\underline{k}) + \rho_{de}(\underline{k})\right] / \epsilon_e(\underline{k}), \tag{9}$$

generalizing the method of Ref. 12. Here, $\rho_{de}$ is the electron charge perturbation due to the electron drift motion *perpendicular* to the transverse electric and the magnetic field. The electron response *parallel* to the electrostatic field is, by definition, built into the dielectric response given by

$$\epsilon_e(k) = \frac{1}{k^2} \underline{k} \cdot \overleftrightarrow{\epsilon}_e \cdot \underline{k}.$$

For oblique wave propagation with $\omega/k_{||} \ll v_e$, $\epsilon_e \to 1 + k^2/k_{\mathrm{De}}^2$ and the electrostatic response comes mainly from the electron motion parallel to the magnetic field, where $v_e$ is the electron thermal speed and $k_{\mathrm{De}}$ the electron Debye wavenumber. In case of almost perpendicular propagation, $\omega/k_{||} \gg v_e$, the electrostatic response diminishes to $\epsilon_e \to 1 + \omega_e^2/\Omega_e^2 \sim 0(1)$, coming from the polarization drift across the magnetic field.

Now the main electron charge perturbation comes from the $E \times B$ drift in response to the transverse electric field. Some of the electron thermal effects could be retained by assigning a magnetic moment $\mu$ to each electron $\boldsymbol{\mu} = \left(m_e v_e^2/2B\right) \hat{z}$ with $m_e$ being the electron mass and then including the electron magnetization current $\mathrm{j}_\mu = \nabla \times n\boldsymbol{\mu}$ due to local magnetic and density gradients.

Returning to Eq. (6), a predicted value for the electric field $\underline{E}^{n-1/2}$ is required to advance the electrons. The one computational cycle for the self-consistent advancing of particles and fields is the following. The ion positions and velocities $x_i^n$ and $v_i^{n-1/2}$ are computed using Eq. (5) with the field values at the previous time step and the ion current density and charge density $\rho_i^n$ and $j_i^{n-1/2}$ are updated. Next, the drift current for the electrons at $t = (n-1)\Delta t$ is also computed using $E_x^{n-1}$ and the velocities $v_e^{n-1}$ from Eq. (6). $E_y$ is advanced by a half step according to

$$E_y^{n-1/2} = \frac{1}{2}\left[E_y^{n-1} + E_y^{n-2}\right] + c\Delta t\left[(\nabla \times B)^{n-1} + j^{n-1}\right] \tag{10}$$

with $j^{n-1} = \frac{1}{2}\left[j_i^{n-1/2} + j_i^{n-3/2}\right] + j_e^{n-1}$. $x_e^n$ and $\rho_e^n$ are updated using $E_y^{n-1/2}$ and the electrostatic field $E_x^n$ is obtained from Poisson's equation and the total charge $\rho_e^n + \rho_i^n$. Using $E_x^{n-1/2} = 1/2\left(E_x^n + E_x^{n-1}\right)$, we obtain the electron drift current $j_e^{n-1/2}$. Inserting the total current into Maxwell's equation, we update the electromagnetic field components $E_y^n$, $B_z^{n+1/2}$. Finally, the corrected value for $E_y^{n-1/2} = 1/2\left[E_y^n + E_y^{n-1}\right]$ is used to reassign the electron positions and the cycle is repeated. A similar algorithm can apply in case of a two-dimensional system $\underline{k} = (k_x, k_y, 0)$.

A considerable reduction in the overall noise level results by following the drifting electrons and suppressing the electron thermal fluctuations. Electron noise is a major inconvenience and smears the physics during low-frequency simulations where the need often arises to resort to interferometry techniques in order to single out the behavior of the frequencies under consideration. Additional (ableit not major) noise reduction comes in the one-dimensional model from the ordinary electromagnetic mode being linearly decoupled and not included in the simulation, reducing the level of electromagnetic fluctuations.

A second benefit from the drift model is that the stability limit on the time step is not tied to the electron characteristic frequencies $\Delta t \lesssim \min\left(\omega_e^{-1}, \Omega_e^{-1}\right)$. The new limits for

stability, if the numerical processes are considered separately, are given by $\Omega_i \Delta t \lesssim 1$ from the equations of particle motion, $\omega_i \Delta t \lesssim 1$ from the electrostatic oscillations and $c\Delta t \lesssim 1$ from Maxwell's hyperbolic equations. The overall stability of the code is determined by the strictest of the above three conditions, often $\Delta t < \Delta c^{-1}$ with $\omega_i^{-1} = 1$ being the time unit. Due to the absence of $k_{||}$, the so-called thermal instability[21] due to particles in resonance with wave aliases introduced by the grid does not appear in the regime where it would otherwise appear for $k_{||} \neq 0$. The ion temperature could be as low as $5 \times 10^{-2}$, allowing a realistic ratio of the ion thermal speed $v_i$ to the speed of light $v_i/c \lesssim 150$ with a reasonable $c(\sim 10)$, provided that the ion Larmor radius $\rho_L = v_\perp/\Omega_i$ remained considerably larger than the grid size $\Delta$.

*B. Plasma model*

We simulate a one-dimensional slab model of a hot plasma embedded in a magnetic field $\underline{B}_0$ along the $z$ direction and varying along the $x$ direction according to $B(x) = b_0/(a+x)$. The pressure and density are uniform across $x$ and no zeroth order current runs along the magnetic field. Thus our system satisfies the trivial magnetohydrodynamic (MHD) equilibrium $\nabla P = j \times B = 0$.

The system is excited by a current driven along the $y$ direction through an infinite antenna sheet on the $yz$ plane placed at distance $x = D$ from the boundary. We apply periodic boundary conditions with electromagnetic wave absorbing boundaries in order to avoid penetration for the waves launched near the one edge from the other edge. This is achieved by advancing the $B$ field, using a masked $E$ field and modifying Eq. (1b) into

$$B^{n+1/2} = B^{n-1/2} - c\Delta t \{\nabla \times (fE)^n\} \tag{11}$$

with the masking function $f$ given in Ref. 22. Equation (11) combined with Eq. (1a) yields the Budden equation[22] in the regions $0 \leq x < D$, $L - D \leq x \leq L$ with wave absorption (non-reflection) at the points $x = 0$ and $x = L$. The natural plasma response is unaffected in the region under investigation $D < x < L - D$. The exciting antenna is placed on $x = D$ or $x = L - D$ for wave launching from the high or low $B$-field side, respectively. Both electrons and ions are recycled through the boundaries. Due to the smallness of the transverse electric field near $x = 0$ and $x = L$, a periodic charge accumulation may

appear at the boundaries, leading to steep electrostatic gradients and local $E \times B$ particle acceleration in the $y$ direction, if the antenna is placed within a distance smaller than a wavelength from the boundary.

It is worth noting that the set of Maxwell's equations combined with the equations of motion are invariant under the scalar transformation

$$q'_\sigma = \lambda_\sigma q_\sigma, \quad m'_\sigma = \lambda_\sigma m_\sigma, \quad n'_\sigma = \lambda_\sigma^{-1} n_\sigma, \quad T'_\sigma = \lambda_\sigma T_\sigma, \tag{12}$$

with $\sigma$ signifying the particle species. This is easily checked by observing that the warm plasma dispersion relation depends on the following plasma parameters $\omega_\sigma$, $\Omega_\sigma, T_\sigma/m_\sigma$ and $\rho_\sigma$, all of which remain invariant under (12). In case of very low minority species concentration, this transformation could be used with $\lambda_\sigma < 1$ in order to increase the number of particles representing minority ions ($\sigma = \beta$) and thus to reduce the accumulation of statistical noise $\sim n_\beta^{-1/2}$ on the modes carried by the minority species ($\beta$) (i.e. Bernstein modes near the minority cyclotron harmonics). However, we find out that this causes a thermal excitation until the equilibration $T'_\alpha = T'_\beta$ is achieved, where $\alpha$ is the majority species. On the other hand, this transformation is appropriate for the cold ($T_e = 0$) drifting electrons that cannot support thermal electrostatic oscillations or absorb energy since $\underline{E} \cdot \underline{v}_e = 0$. Setting $\lambda_e = 4$ cuts the number of particles representing electrons to $1/4$, reducing the size of the code without any increase on the noise level or signs of thermal excitation.

## III. Theory for Mode Conversion in a Two-Ion Species Plasma

A fast magnetosonic wave of frequency $\omega$ propagating nearly perpendicular to the magnetic field in a two-ion species plasma will undergo partial mode conversion into a short wavelength electrostatic mode near the layer $x_{mc}$ defined by

$$\omega = \omega_{IH}\left(x_{mc}\right) \equiv \Omega_\alpha \left[\left(\frac{\omega_\beta^2}{\omega_\alpha^2} + \frac{\Omega_\beta^2}{\Omega_\alpha^2}\right) \Big/ \left(1 + \frac{\omega_\beta^2}{\omega_\alpha^2}\right)\right]^{1/2} \tag{13}$$

with $\omega_\alpha$, $\omega_\beta$ the plasma frequencies, and $\Omega_\alpha$, $\Omega_\beta$ the cyclotron frequencies of the majority and minority ion species, respectively. Note that the ion-hybrid frequency $\omega_{IH} \to \Omega_\beta$ as the minority concentration $n_\beta \to 0$. The local dispersion relation plotted in Fig. 2 shows the existence of two branches $k_i^2(x,\omega)(i = 1,2)$ of equal real parts near the mode conversion zone; further away from resonance, these branches could be identified as the fast magnetosonic mode and the minority ion Bernstein mode.

As the WKB approximation, on which Fig. 2 is based, fails near the mode conversion region, a solution of the full wave propagation equation is required to study the effect of mode conversion. The results of the extensive analytic work by Swanson,[2,4,5] as well as by Jacquinot[3] and Perkins,[6] including finite $k_\|$, Landau damping and toroidal effects, can be formulated in terms of a transfer matrix, connecting the coefficients between the two asymptotic wave solutions at $x = \pm\infty$ (with $x$ measured from the resonance $x = 0$),

$$e^{+iz} + Re^{-iz} \xleftarrow{-\infty} \qquad \xrightarrow{+\infty} Te^{iz} + Ce^{i\frac{2}{3}\lambda|z|^{3/2}} \tag{14}$$

where evanescent terms have been omitted in Eq. (14). In the simple case with $k_\| = 0$ and linear profile for the plasma parameters, the reflection transmission and mode conversion coefficients are given by

$$R = 0, \quad T = e^{-\eta}, \quad C = -\left(1 - e^{-2\eta}\right) \tag{15}$$

for incidence from the high field side and

$$R = -\left(1 - e^{-2\eta}\right), \quad T = e^{-\eta}, \quad C = -e^{-\eta}\left(1 - e^{-2\eta}\right) \tag{16}$$

for incidence from the low field side where $\lambda$ and $\eta$ depend on the plasma parameters. In particular, $\eta$ is roughly proportional to the relative minority concentration $n_\beta/n_\alpha$ and was

shown to be much larger than 1 for typical thermonuclear plasmas.[2] Then examination of the coefficients in Eqs. (15) and (16) shows a major difference between the two cases; as for high field side incidence, the incoming wave is primarily mode converted to the slow electrostatic mode, while for low field side incidence it is primarily reflected away from the mode conversion region.

Energy conservation yields the energy fraction extracted from the incident fast magnetosonic as

$$\Delta E = 1 - |R|^2 - |T|^2 = \Delta E_{abs} + \Delta E_{mc}. \tag{17}$$

$\Delta E_{abs}$ is the fraction of energy absorbed via the combined minority ion cyclotron and the majority first cyclotron harmonic Landau damping as for small minority concentration of hydrogen in deuterium $\omega_{IH} \cong \Omega_H \cong 2\Omega_D$. $\Delta E_{mc}$ is the fraction of energy carried away by the electrostatic mode generated by conversion, $\Delta E_{mc} = |C|^2 \left(1 - e^{-2\eta}\right)^{-1}$. Since the energy in the electrostatic branch cannot leave the plasma and it is eventually absorbed by electrons, the mode conversion and local ion cyclotron absorption are the two crucial aspects in determining energy deposition during ion-hybrid heating. A detailed analytic and computational study has recently been performed by Colestock and Kashuba[23] by utilizing the non-uniform plasma dielectric response tensor and solving numerically the resulting set of coupled differential equations. Their results, along with the previous work on the subject, are included in the review paper by Swanson.[24]

There is a considerable difference in local absorption, depending on whether the wave is incident from the high or from the low field side. In case of incidence from the low field side, the wave first encounters the minority cyclotron resonance before the two-ion hybrid resonance. Direct minority heating occurs through the cyclotron resonance due to the left-hand circularly polarized component $E_+$ in the magnetosonic mode.[1] In the opposite case of incidence from the high field side the wave encounters the two-ion hybrid resonance first and must be tunneled to the minority cyclotron regime, as seen in Fig. 2, being at the same time mode-converted to an electrostatic mode. Nevertheless, direct ion heating has been observed experimentally[7-8] near the two-ion hybrid layer even for cases with the minority cyclotron resonance located outside the plasma. This heating cannot be accounted for by the linear theory demanding $(\Omega - \omega)/k_{\|} \leq v_{\min}$ for resonance and

suggests the existence of non-linear wave particle interactions for energy transfer.

In order to focus on the non-linear effects on heating, we simulate wave propagation with $k_{||} = 0$. Then local energy absorption due to Landau damping cannot take place. However, non-linear wave particle interaction provides additional heating mechanisms and strong energy absorption is actually observed. There can be two channels for energy transfer from the wave to the particles.

*A. Direct absorption*

Particle heating due to non-linear coherent interaction can be understood in the approximation of a large amplitude monochromatic wave interacting with the ions. The adiabatic limit with the bouncing frequency $\omega_b \gg \gamma$, the growth rate for the wave, is assumed. Particles can be non-linearly trapped, even with $k_{||} = 0$, through a sequence of correlated kicks in velocity $\Delta v$ received during each cyclotron period when the wave frequency is close enough to a cyclotron harmonic

$$\left|\frac{\omega - n\Omega_\alpha}{n\Omega_\alpha}\right| < \left[\frac{J_n'(k\rho_L)}{k\rho_L}\right]_{\max} \frac{e}{m} \frac{E_\perp}{\left(\Omega_\alpha/k_\perp\right)^2} k_\perp. \tag{18}$$

Non-stochastic heating occurs[25] as the trapped particles circulate with different bouncing frequencies around islands in phase space, causing a flattening of the distribution function across an island in a similar manner as in case of damping of electrostatic oscillations in an unmagnetized plasma.

Stochastic acceleration by a monochromatic wave can also occur[26] for wave amplitude above the stochasticity threshold,

$$\frac{e}{m} \frac{E_\perp k_\perp}{\left(\Omega_\alpha/k_\perp\right)^2} \gtrsim 1, \tag{19}$$

because the kicks in velocity received from the wave become uncorrelated. The term stochastic implies that the decorrelation time among kicks $\tau_d$ is much shorter than the bouncing period $\omega_b$, $\omega_b \tau_d \ll 1$, whether decorrelation is caused by a single monochromatic wave or a wide band of fluctuations (see below). In case of magnetosonic modes, a large $B_z/B_0$ unacceptable for practical applications results if one tries to satisfy the above condition. However, low level turbulence can considerably lower the amplitude required for stochasticity.

*B. Indirect absorption*

The pump wave can interact with the background fluctuations and through non-linear cascades it can enhance fluctuations far above the thermal equilibrium level. Heating occurs through the randomization of the particle trajectories and the resulting turbulent diffusion in their distribution function. Stochastic heating caused by a wide fluctuation spectrum was originally studied in the context of the quasilinear theory. It has been shown employing the methods of Dupree,[27] Weinstock,[28] and Matsumoto[29] that the heating rate for waves propagating perpendicularly to a uniform magnetic field is given by

$$\frac{dK}{dt} \sim \int dk \omega_{pi}^2 \frac{k^2 c^2}{B^2} \left\langle E^2(k) \right\rangle b(k, \omega(k))$$

where $\left\langle E^2(k) \right\rangle$ is the (ensemble) average spectral density and $b(k, \omega(k))$ a weighting factor peaking near $\omega(k) \sim \Omega_i$. This mechanism has been studied numerically for the one-ion species ICRH case in Ref. 30.

The fluctuation level at saturation has yet to be determined that is reached when the rate of non-linear energy transfer to short wavelengths is balanced by the rate of ion heating. Depending on the parameters, it can be one of the main issues determining energy absorption during ICRH. Since during actual heating conditions of our simulation we have the presence of both a high amplitude pump wave and a turbulent background, the interplay between the above two heating mechanisms must be examined in connection with the observed power spectrum for the wave field.

A word must be said here about how realistically our one-dimensional model can simulate actual heating. The fact that in a real experiment the launched waves may occupy a finite segment of the torus seems to question the validity of our results as we simulate a wave that extends to $\pm\infty$ in the $z$ direction. However, given that the passage time of a particle through the finite interaction regime is $\tau_p$, we can divide the trajectory of one particle in an infinitely extending wave in segments of length $\tau_p$. If the decorrelation time $\tau_d$ is shorter than $\tau_p$, then $n$ segments of the one particle trajectory are statistically independent and equivalent with the one passage through a finite interacting regime of $n$ independent particles from the average taking standpoint.

## IV. Numerical Results

A series of runs are performed using our code to numerically investigate the physics of the ion–ion hybrid mode conversion for wave propagation perpendicular to the magnetic field in a two-ion species plasma with deuteron ($D$) as majority and hydrogen ($H$) as minority. Lengths are normalized to grid size $\Delta$ and times to the deuteron plasma frequency for 100% deuterium $\omega_D^{-1}$. The grid size is related to the Debye length through $\Delta = \lambda_D \tilde{v}^{-1}$ with the normalized temperature $\tilde{T}$ and velocity $\tilde{v}$ related by $\tilde{T} = kT/m_D\left(\Delta\omega_D\right)^2 = \tilde{v}^2$. Electric fields are measured in units of $\frac{m_D}{e}\omega_D\Delta$. We typically simulated a length $L$ of 1024 grid points using 40,000 ions and only 10,000 particles representing electrons with effective charge equal to 4 as explained in the previous section. We varied the ratio $\omega_D/\Omega_D$ in the range from 3.33 to 36 for two concentration ratios $n_H/n_D = 1$ and $n_H/n_D = 1/4$. The speed of light is typically $\tilde{c} \sim 10$, the ion thermal speeds are in the range between 1/150 and 1/200 of the light speed and the ratio of ion to magnetic pressure varies between 1% and 9% for various runs.

We typically use 512 spectral components for the electrostatic and 256 for the electromagnetic modes of the fields. A typical time averaged spectral density profile $\left\langle E^2(k)\right\rangle$ for the thermal fluctuations is shown in Figs. 3(a)–3(c), the averaging time $T$ being 5 deuteron cyclotron periods. The main overall noise contribution comes from the short wavelength regime of the electrostatic oscillations as seen in Fig. 3(a), while the electromagnetic field components yield the main contribution in the long wavelength regime, Figs. 3(b) and 3(c). Using Fourier analysis of the field data in time, we observe frequencies up to $20\Omega_D$, each frequency usually associated with two distinct groups of wavenumbers, thus accounting for the two distinct roots of the dispersion relation shown in Fig. 2.

For wave incidence from the high field side, the pump frequency was set at $\omega_{\text{pump}} = \omega_{IH}(3/4L)$ with $\omega_{IH}$ given by Eq. (13), arranged to place the mode conversion layer at $x_{mc} = 3/4L$. The time span simulated was typically 10 to 20 deuteron cyclotron periods, enough for wave propagation from boundary to boundary. The antenna current is limited by the requirement $B_z/B_0 \lesssim 5\%$ in order to avoid considerable wave steepening and strong non-linear harmonic generation. Such phenomena are observed during runs with high antenna current. As the electric field components scale as $E_x \sim E_y \cong \frac{v_A}{c}B_z$, the

wave electrostatic field is moderately above the electrostatic thermal fluctuation level for runs with high $\omega_D/\Omega_D \cong c/v_A$ ratio; the pictures of the $E_y$ and $B_z$ waveforms are much clearer due to the lower level of electromagnetic noise in the present simulation. The field profiles are obtained without resorting to interferometry, a technique used to unmask the low-frequency information[31] in case that full electron dynamics is used. Results obtained for $\omega_D/\Omega_D = 9.32$, $\tilde{c} = 12$, $c/v_D = 120$ and $n_H/n_D = 1/4$ are shown in Figs. 4(a)–4(c).

The sudden reduction in the electromagnetic energy flux (the Poynting vector) that occurs near the middle of the plasma slab, Fig. 4(d), is an indication of the partial mode conversion of the incoming electromagnetic energy associated with the fast magnetosonic mode into the electrostatic branch of the ion–ion hybrid mode. Because the system boundaries are within finite distance from the mode conversion layer $x_{mc}$, the asymptotic form of the waves in Eq. (14), showing wavelength separation for the two modes, cannot be observed and the coefficients $R$, $T$, and $S$ are not directly measurable. Nevertheless, this reduction in electromagnetic energy flux cannot be attributed to any strong localized absorption by particles as it is checked from the phase space plots Figs. 5(a)–5(d), plots of the absorbed power density $\mathbf{j} \cdot \mathbf{E}$, and the cyclotron frequency profiles for the two-ion species, Fig. 1. Therefore, the reduction in the Poynting vector can be used to estimate the percentage of the mode conversion taking place near the ion–ion hybrid resonance layer. This method of estimate yields a surprisingly high conversion coefficient of 90% or higher for a wide range of densities between $\omega_D/\Omega_D = 3.33$ and $\omega_D/\Omega_D \cong 40$. Finite Larmor radius effects combined with the inhomogeneity place the mode conversion layer before $x_{mc}$ that is derived by the WKB approximation. An analogous effect is observed during upper hybrid mode conversion simulation and is explained analytically by the inclusion of spatial derivatives of odd order in the wave propagation differential equation. Both high conversion efficiency and relative insensitivity on the $\omega_D/\Omega_D$ ratio may be due to finite amplitude (non-linear) effects and differ from the linear results of Ref. 23 showing a strong decrease in conversion efficiency for $\omega_D/\Omega_D < 40$.

The time evolution of the field energy stored in $E_x$, $E_y$ and $B_z$ is shown in Figs. 6(a)–6(c). There is a clear break in the rate of increase of the field energy in all three curves around $t \sim 375\omega_D^{-1}$, corresponding to the time when the wave propagates through the

plasma and starts being absorbed at the opposite-to-the-antenna boundary. At this point a steady state is reached with the energy input of the antenna balanced by particle and boundary absorption. However, the energy of electrostatic fluctuations keeps increasing as the ion temperature increases and it accounts for the slow field energy increase in Fig. 6(a) after $t \sim 375\omega_D^{-1}$. The energy of electromagnetic fluctuations remains always much smaller than the energy of the pump wave.

The time evolution of the kinetic energy is shown in Figs. 7(a)–7(c). The growth is linear in time and the same behavior is repeated in all of our runs with different parameters. A fraction of this energy increase is attributed to the linear particle response to the wave penetrating deeper into the plasma. However, linear theory predicts that the kinetic energy be saturated along with the wave energy and be of the same magnitude as that. Instead, the observed rate of increase is not affected by the field energy saturation, suggesting that the non-linear particle response is the main mechanism for the intense heating. The velocity distributions for majority and minority at the beginning and at the end of the run are shown in Figs. 8(a)–8(f).

The percentage increase in kinetic energy for a time interval equal to 100 deuteron plasma periods with a constant antenna current is shown in Table I for various plasma parameters. Some conclusions about the dependence of the direct ion heating on the plasma parameters can be drawn by examining these simulation data:

(a) The absolute increase in both majority and minority ion energies is relatively insensitive to the plasma temperature. From lines 1 to 3 it is shown that an increase in $T$ by a factor of 3 reduces the minority heating by 20%, while it does not significantly affect the majority absorption. Therefore, the percentage increase in energy is roughly inversely proportional to the initial kinetic energy and scales as $T^{-1}$.

(b) The overall energy absorption tends to increase for increased minority concentration for fixed temperature and fixed ratio $\omega_D/\Omega_D$. The percentage change in the minority energy decreases with increasing minority concentration as seen by comparing line 2 with line 4 and line 6 with line 7. This is expected as the ion–ion hybrid frequency drops from $0.87\Omega_H$ to $0.70\Omega_H$ for hydrogen concentration increasing from 20% to 50%. This loss in minority heating is more than made up for by the increasing majority heating as the

ion–ion hybrid approaches the 3/2 deuteron cyclotron harmonic, $\omega_{IH} \rightarrow 1.41\Omega_D$ for 50% hydrogen.

(c) The dependence of energy absorption on the ratio $\omega_D/\Omega_D$ for fixed temperature and antenna current is deduced from lines 3, 5, 6. Energy absorption by both majority and minority species tends to increase with decreasing ratio $\omega_D/\Omega_D$. However, decreasing $\omega_D/\Omega_D$ with constant antenna current $I$ results in increasing the stored energy in the fields scaling as $\langle E^2 \rangle \sim \frac{4\pi I}{c}\frac{v_{ph}}{c} \cong \frac{4\pi I}{c}\left[\omega_D/\Omega_D\right]^{-1}$ as shown in column of Table I. We may extrapolate the results in each line of Table I as to correspond to a constant electric field energy rather than a constant current through the antenna by making the reasonable assumption, characteristic of the diffusive process, that with all other parameters held constant, $\Delta K$ scales proportionally to $\langle E^2 \rangle$. The overall net change in kinetic energy under constant $\langle E^2 \rangle$ and constant $n_H/n_D$ now tends to increase with increasing $\omega_D/\Omega_D$, from $\Delta K_t = 129.0$ to 150.0 to 209.0 to 265.5 as $\omega_D/\Omega_D$ goes from 3.33 to 6.66 to 9.32 to 20.65 and $\int \left\langle \tilde{E}^2 \right\rangle dx$ remains around 26 in the normalized units.

So far the case of wave incidence from the high field side (HFS) has been considered. Plots of phase space, velocity distribution, field profiles for the LFS case with $\omega_D/\Omega_D = 6.66$, $\tilde{c} = 15$, $c/v_D = 150$, and $n_H/n_D = 1/4$ are shown in Figs. 9–13. The Poynting flux in Fig. 10(d) looks similar to the one for the high field side case. Here, however, the reduction in the electromagnetic energy flux must be attributed to reflection rather than to mode conversion. This is supported by the plot of the electrostatic field profile Fig. 10(a) showing very small coherent response above noise level compared to the high field side counterpart Fig. 4(a). Data for the above plots are shown in line 11. Comparison with the results in line 5 for HFS incidence with identical plasma parameters shows a doubling in the heating rate of the minority hydrogen compared to the high field side incidence. However, the majority heating is quite small and the overall heating is smaller than that in case of high field incidence. Strong hydrogen heating is expected as the wave encounters the cyclotron resonance layer before the mode conversion and agrees with experimental observation of fast minority ion tails. A much smaller heating of majority ions (compared to the case of high field side launching) has also been observed experimentally. This is rather surprising, considering the fact that $\omega = \Omega_H$ is also the first harmonic of deuteron $\omega = 2\Omega_D$. The

majority heating during the LFS launch is found to be very small, even compared to the heating produced by a HFS-launched magnetosonic mode of frequency $\omega = 3/4\Omega_D$, below the deuteron cyclotron frequency everywhere in the simulation regime and far away from mode conversion (line 10). This tendency for selective minority heating during LFS incidence showed clearly in an extended run with strong antenna current when an increase of minority temperature $T_H$ by a factor $T_H/T_H(0) = 6.5$ within time $t = 1142\omega_D^{-1}$ was realized, compared to a majority change in temperature of only $T_D/T_D(0) = 1.8$. It is suggested to the authors that the resulting large difference in temperature between the two-ion species may trigger two-ion velocity space instabilities,[32] resulting in fast heating of the majority ions on a time scale much shorter than the effective collision time. This would require $T_H/T_D \gtrsim 10$ and is left as a subject for future investigation.

Typical spectral density profiles $\langle E^2(k)\rangle$, where the time average has been taken during the last one-third of the simulation period, appears in Figs. 14(a)–(c) and 15(a)–(c). The presence of a strong nearly monochromatic component on top of an extended noise background clearly suggests that both mechanisms of direct and indirect energy absorption can co-exist and interfere with each other during the wave damping. A considerable amplification of the fluctuation level above that of the thermal equilibrium is seen by comparing Fig. 3 with Figs. 14 and 15. Turbulent diffusion, therefore, contributes to indirect heating.

Direct heating from the strong pump wave at a first glance may appear unfavored. For considerable non-stochastic heating, a large fraction of the ions must be trapped. The trapping condition, Eq. (18), is written in the dimensionless code parameters as

$$\left|\frac{n_\sigma\Omega_\sigma - \omega_{\text{pump}}}{n_\sigma\Omega_\sigma}\right| < \left[\frac{J'_{n_\sigma}\left(\tilde{k}\tilde{\rho}\right)}{\tilde{k}\tilde{\rho}}\right]_{\max}\left(\frac{\tilde{\omega}_D}{\tilde{\Omega}_D}\right)^2 \tilde{k}\tilde{E}_x$$

with $n_\sigma = 1$ for $H$, $n_\sigma = 2$ for $D$, yielding $\tilde{E}_x > \left|1 - \frac{\omega_{\text{pump}}}{n_\alpha\Omega_\alpha}\right|\left(\tilde{\Omega}_D/\tilde{\omega}_D\right)^2 10\tilde{k}$. For concentration ratio $n_H/n_D = 1/4$ we have $\omega_{\text{pump}} = 1.73\Omega_D$ and $\tilde{E}_x > 2\times 10^{-2}$ near resonance. The typical values for $\tilde{E}_x$ in our runs are not well above this requirement to guarantee extensive trapping; furthermore, the coherent motion can be destroyed in the presence of a noise background. The threshold for stochastic heating on the other hand is weakly

dependent on $\omega$ and given by

$$\tilde{E}_x \gtrsim \left(\frac{\tilde{\Omega}_D}{\tilde{\omega}_D}\right)^2 10^1 \sim 10^{-1}.$$

In order to exceed these thresholds, $\tilde{B}_z/\tilde{B}_0$ must become large $\sim \frac{c}{v_A}\frac{\tilde{E}_x}{\tilde{B}_0}$ and unacceptable for real applications. However, Eq. (19) is obtained in the simplified limit of a single monochromatic wave. It is conceivable that the presence of a low level turbulence will act as a stochasticity pool of modes that decorrelate the phase of the particles between two successive jumps $\Delta v$ induced by the wave that acts as the energy pump. The expected threshold for stochastic diffusion in this case should be much lower than in Eq. (19). Typical surface of section plots for individual particles appear in Figs. 16(a)–(d), demonstrating in fact the stochastic character of motion. In case of non-stochastic (regular) motion, the surfaces of section, generated by recording the momentum $p_x$ and $p_y$ of an ion at time intervals of half wave period $\pi/\omega$, should show periodic island structure.

For a comparison's sake we show the results of a stochastic heating case in the phase space plot of Fig. 17, where the electric field of the pump is much larger than the stochasticity threshold. These results simulate a large amplitude wave propagating through a pure hydrogen plasma to the upper hybrid mode conversion regime, characterized by the short wavelength near the middle of the plot. The blow up in velocities is localized around the resonant layer $\omega \sim \Omega_e$ near $x/L \sim 0.25$ rather than near the mode conversion layer at $x/L \sim 0.50$. Returning to the ion cyclotron heating, it is estimated from Figs. 14 and 15 that the energy content of the pump wave is of the same order as the energy contained in the above equilibrium part of the fluctuations. Therefore, each of the limiting cases discussed previously would by itself provide a poor quantitative account of the heating rate. Further research of the role played by non-linear mechanisms during ion cyclotron heating has to be carried out in light of our numerical study showing several heating mechanisms participating.

**Acknowledgements**

We would like to thank Dr. V. Demchenko of Kharkov, USSR, for discussions on Ref. 32. The work was supported by the U. S. Department of Energy Contract #DE-FG05-80ET-53088.

## References


1. T. H. Stix, Nucl. Fusion **15**, 737 (1975).
2. D. G. Swanson, Phys. Rev. Lett. **36**, 316 (1976).
3. J. Jacquinot, B. D. McVey and J. E. Scharer, Phys. Rev. Lett. **39**, 88 (1976).
4. Y. C. Ngan and D. G. Swanson, Phys. Fluids **20**, 1920 (1977).
5. D. G. Swanson, Nucl. Fusion **20**, 949 (1980).
6. F. W. Perkins, Nucl. Fusion **17**, 1197 (1977).
7. TFR Group, in *Proceedings of the Eight International Conference on Plasma Physics and Controlled Nuclear Fusion Research*, 1980 (IAEA, Vienna 1981), Vol. 2, p. 75.
8. D. Hwang, R. E. Chrien, P. Colestock, S. L. Davis, R. J. Goldston, J. C. Hosea, H. Hsuan, R. Kaita, S. S. Medley, D. Mueller, J. D. Strachan, S. Suckewer, H. R. Thompson, and G. Zankl, in *Proceedings of the International Conference in Plasma Physics* (Fusion Research Association of Japan, Nagoya 1980), Vol. II, p. 213.
9. A. B. Langdon and B. Lasinski, in **Methods in Computational Physics**, B. Alder, S. Fernbach, M. Rotenberg, and J. Killeen, eds. (Academic, New York, 1976), Vol. 16, p. 327.
10. A. T. Lin, J. M. Dawson, and H. Okuda, Phys. Fluids **17**, 1995 (1974).
11. A. T. Lin, C. C. Lin, and J. M. Dawson, Phys. Fluids **25**, 646 (1982).
12. H. Okuda, J. M. Dawson, A. T. Lin, and C. C. Lin, Phys. Fluids **21**, 476 (1978).
13. C. C. Lin, A. T. Lin, and H. Okuda, Phys. Fluids **22**, 2331 (1979).
14. J. Byers, B. I. Cohen, W. C. Condit, and J. D. Hanson, J. Comp. Phys. **27**, 363 (1978).
15. D. W. Hewett and C. W. Nielson, J. Comp. Phys. **29**, 219 (1978).
16. C. W. Nielson and H. R. Lewis, in **Methods in Computational Physics**, B. Alder, S. Fernbach, M. Rotenberg, and J. Killeen, eds. (Academic, New York, 1976), Vol. 16, p. 367.
17. J. Busnardo-Neto, P. L. Pritchett, A. T. Lin, and J. M. Dawson, J. Comp. Phys. **23**, 300 (1977).
18. W. W. Lee and H. Okuda, J. Comp. Phys. **36**, 870 (1976).

19. C. Z. Cheng and H. Okuda, in *Proc. Eighth Numerical Simulation Conference* (U. S. Department of Energy, Monterey, 1978), p. PE-2.
20. J. Geary, J.-N. Leboeuf, and T. Tajima, in *Proc. Eleventh Numerical Simulation Conference* (U. S. Department of Energy, Quebec, 1985), p. 1B-10.
21. C. K. Birdsall and A. B. Langdon, in **Plasma Physics via Computer Simulations** (McGraw-Hill, New York, 1985), pp. 177–181.
22. T. Tajima and Y. C. Lee, J. Comp. Phys. **42**, 406 (1981).
23. P. L. Colestock and R. J. Kashuba, Nucl. Fusion **23**, 763 (1983).
24. D. G. Swanson, Phys. Fluids **28**, 2645 (1985).
25. S. Riyopoulos, J. Plasma Phys. **196**, 444 (1986).
26. J. Y. Hsu, Phys. Fluids **25**, 159 (1982).
27. T. H. Dupree, Phys. Fluids **9**, 1773 (1966).
28. J. Weinstock, Phys. Fluids **12**, 1045 (1969).
29. M. Matsumoto, J. Phys. Soc. Japan **42**, 1366 (1977).
30. M. Matsumoto, S. Takeuchi, and K. Sakai, in **Fundamentals of Heating Techniques**, ed. S. Tanaka (Ministry of Education, Tokyo, 1983), p. 313.
31. H. Abe, R. Itatani, and H. Momota, Phys. Fluids **22**, 1533 (1979).
32. V. L. Sizonenko and K. N. Stepanov, Sov. Phys. JETP Lett. **8**, 363 (1968) [ZhETF Pis. Red. **8**, 92 (1968)].

## Figure Captions

Fig. 1: The one-dimensional plasma model used in our simulations. Shown are the ion cyclotron frequency profiles and the two-ion hybrid frequency profiles and the two-ion hybrid frequency $\omega_{IH}$ plotted against the distance $\underline{x} = x/L$ from the two-ion hybrid resonance layer. The line $\omega = \omega_{\text{pump}}$ matches the local $\omega_{IH}$ at distance $\underline{x} = 3/4L$ from the origin.

Fig. 2: The real part $k_\perp^2$ for the two branches of the dispersion relation near the mode conversion for pure perpendicular wave propagation, according to WKB theory. The parameters are the same as in Fig. 3.

Fig. 3: The time-averaged spectrum of the thermal fluctuations for (a) $\left\langle \tilde{E}_x^2(k_n) \right\rangle$ (b) $\left\langle \tilde{E}_y^2(k_n) \right\rangle$ (c) $\left\langle \tilde{B}_z^2(k_n) \right\rangle$. The wave vector $k_n = n\frac{2\pi}{L}$. The plasma parameters in Figs. 3 through 8 are $n_H/n_D = 1/4$, $\tilde{v}_x = 0.10$, $\tilde{c} = 12$, and $\omega_D/\Omega_D = 9.32$.

Fig. 4: The field profiles at time $t = 628\omega_D^{-1}$ during incidence from the high field side: (a) $E_x$ (b) $E_y$ (c) $B_z$ (d) Poynting (energy flux) vector. The position of the resonance $\omega_{\text{pump}}^2 = \omega_{IH}^2(x)$ in cold plasma theory is at $\tilde{x}_{mc} = 750$. The abrupt flip of $P$ in (d) at $\tilde{x} = 80$ is due to the antenna located at that point.

Fig. 5: Plots of the ion phase space at $t = 628\omega_D^{-1}$ for the same parameters as in Fig. 3. Most of the observed activity takes place on the left of the mode conversion layer. (a) $v_x$, $x$ and (b) $v_y$, $x$ for deuteron, (c) $v_x$, $x$ and (d) $v_y$, $x$ for hydrogen.

Fig. 6: Time evolution of the total energy in the (a) longitudinal electric (b) transverse electric (c) magnetic fields.

Fig. 7: Time evolution of the (a) deuteron (b) hydrogen and (c) total kinetic energy.

Fig. 8: The (unnormalized) velocity distributions over the simulation volume for (a) deuteron (b) hydrogen at $t = 0$, (c) deuteron (d) hydrogen at $t = 628\omega_D^{-1}$. The velocity distribution for (e) deuteron (f) hydrogen in the strong interaction regime $L/3 \lesssim x \lesssim 2L/3$ shows more heating than (c) and (d), respectively.

Fig. 9: Plot of ion phase space at time $t = 628\omega_D^{-1}$. Same notation as in Fig. 5.

Fig. 10: Field profiles for incidence from the low field side at $t = 628\omega_D^{-1}$, (a) $\tilde{E}_x(x)$ (b) $\tilde{E}_y(x)$ (c) $\tilde{B}_z(x)$ and (d) Poynting flux vector. The plasma parameters in Figs. 9 through 13 are $n_H/n_D = 1/4$, $\tilde{v}_x = 0.10$, $\tilde{c} = 15$ and $\omega_D/\Omega_D = 6.66$. The hydrogen cyclotron layer is at $\tilde{x}_{ch} \cong 800$ and the cold plasma ion–ion hybrid layer is at $\tilde{x}_{mc} = 550$.

Fig. 11: Velocity distribution over the simulation volume at time $t = 628\omega_D^{-1}$ for (a) deuteron (b) hydrogen. Velocity distributions in the regime $0.5 \lesssim x/L \lesssim 0.9$ are shown in (c) deuteron and (d) hydrogen. Initial ion distributions are the same as in Figs. 8(a) and 8(b), respectively.

Fig. 12: Time evolution of the energy stored in (a) electrostatic (b) transverse electric and (c) magnetic fields during wave incidence from the low field side.

Fig. 13: Time evolution of the kinetic energy for (a) deuteron (b) hydrogen (c) total during wave incidence from the low field side.

Fig. 14: The time-averaged spectral density during the final field saturation stage for the high field side incidence (a) $\left\langle \tilde{E}_x^2(k_n) \right\rangle$ (b) $\left\langle \tilde{E}_y^2(k_n) \right\rangle$ (c) $\left\langle \tilde{B}_z^2(k_n) \right\rangle$.

Fig. 15: Same as in Fig. 14 but for the low field side incidence.

Fig. 16: Typical surfaces of section for ions near the midplane of the simulation regime showing stochastic acceleration. The coordines $p_x$, $p_y$ are recorded every half wave period $\pi/\omega_{\text{pump}}$, and the parameters are the same as in Fig. 3. Total elapsed time is 628 $\omega_D^{-1}$.

Fig. 17: Large amplitude stochastic heating simulation. (a) phase space plot. The upper hybrid resonance is at $\tilde{x} = 125$, however, strong electron heating is observed near the electron cyclotron resonance at $\tilde{x} = 75$. (b) A typical surface of section for an electron near the resonant regime.

## Table I

### Simulation Results

| $n_H/n_D$ | $\int \lvert\tilde{E}\rvert^2 dx$ | $\frac{\omega_D}{\Omega_D}$ | $\tilde{v}_x = \tilde{v}_y$ | $\tilde{c}$ | $\Delta\tilde{K}_D$ | $\Delta\tilde{K}_H$ | $\Delta\tilde{K}_{\text{tot}}$ | $\%\left(\frac{\Delta K}{K_0}\right)_D$ | $\%\left(\frac{\Delta K}{K_0}\right)_H$ | $\%\left(\frac{\Delta K}{K_0}\right)_{\text{tot}}$ |
|---|---|---|---|---|---|---|---|---|---|---|
| 1. 1/4 | 5.25 | 18.85 | .060 | 10 | 63.5 | 29.7 | 93.2 | 55.7 | 102.5 | 65.1 |
| 2. 1/4 | 7.30 | 18.85 | .075 | 10 | 61.6 | 25.7 | 87.3 | 37.5 | 58.2 | 41.0 |
| 3. 1/4 | 8.50 | 20.65 | .100 | 10 | 65.3 | 23.2 | 88.5 | 20.6 | 29.1 | 22.2 |
| 4. 1/1 | 8.35 | 18.85 | .075 | 10 | 74.3 | 43.3 | 117.6 | 67.5 | 38.6 | 52.9 |
| 5. 1/4 | 15.10 | 9.32 | .100 | 12 | 79.0 | 43.0 | 122.0 | 24.8 | 53.8 | 30.7 |
| 6. 1/4 | 25.60 | 6.66 | .100 | 15 | 93.5 | 56.4 | 149.9 | 29.2 | 70.4 | 37.5 |
| 7. 1/1 | 23.80 | 6.66 | .100 | 15 | 125.0 | 71.4 | 196.4 | 63.0 | 35.9 | 49.4 |
| 8. 1/4 | 45.00 | 3.32 | .200 | 15 | 156.0 | 70.0 | 226.0 | 12.3 | 21.9 | 14.2 |
| 9.(a) 1/4 | 2.05 | 36.50 | .050 | 10 | 12.6 | 8.4 | 21.0 | 15.9 | 41.8 | 21.2 |
| 10.(b) 1/4 | 16.00 | 9.32 | .100 | 12 | 79.0 | 9.0 | 88.0 | 24.8 | 11.2 | 22.1 |
| 11.(c) 1/4 | 23.30 | 6.66 | .100 | 15 | 15.0 | 97.0 | 122.0 | 4.8 | 121.3 | 28.1 |

(a) $j_{\text{antenna}} = 1.25$

(b) $\omega_{\text{pump}} = (3/4)\Omega_D$ at $\tilde{x} = 0.75$, no mode conversion.

(c) Incidence from the low field side.

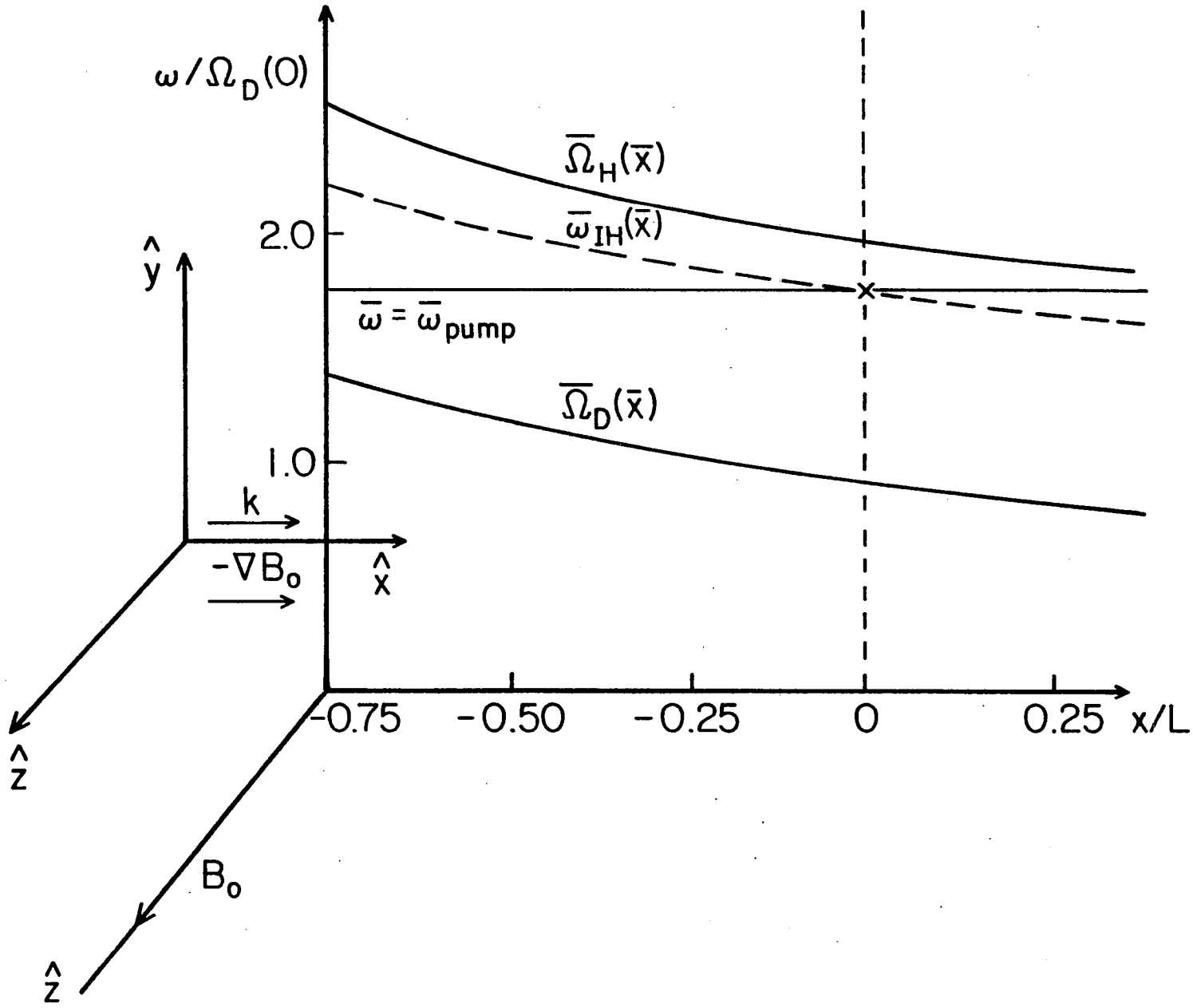
$\omega/\Omega_D(0)$
$\bar{\Omega}_H(\bar{x})$
$\bar{\omega}_{IH}(\bar{x})$
2.0
$\hat{y}$
$\bar{\omega} = \bar{\omega}_{pump}$
$\bar{\Omega}_D(\bar{x})$
1.0
k
$-\nabla B_o$
$\hat{x}$
-0.75
-0.50
-0.25
0
0.25
x/L
$\hat{z}$
$B_o$
$\hat{z}$

Fig. 1

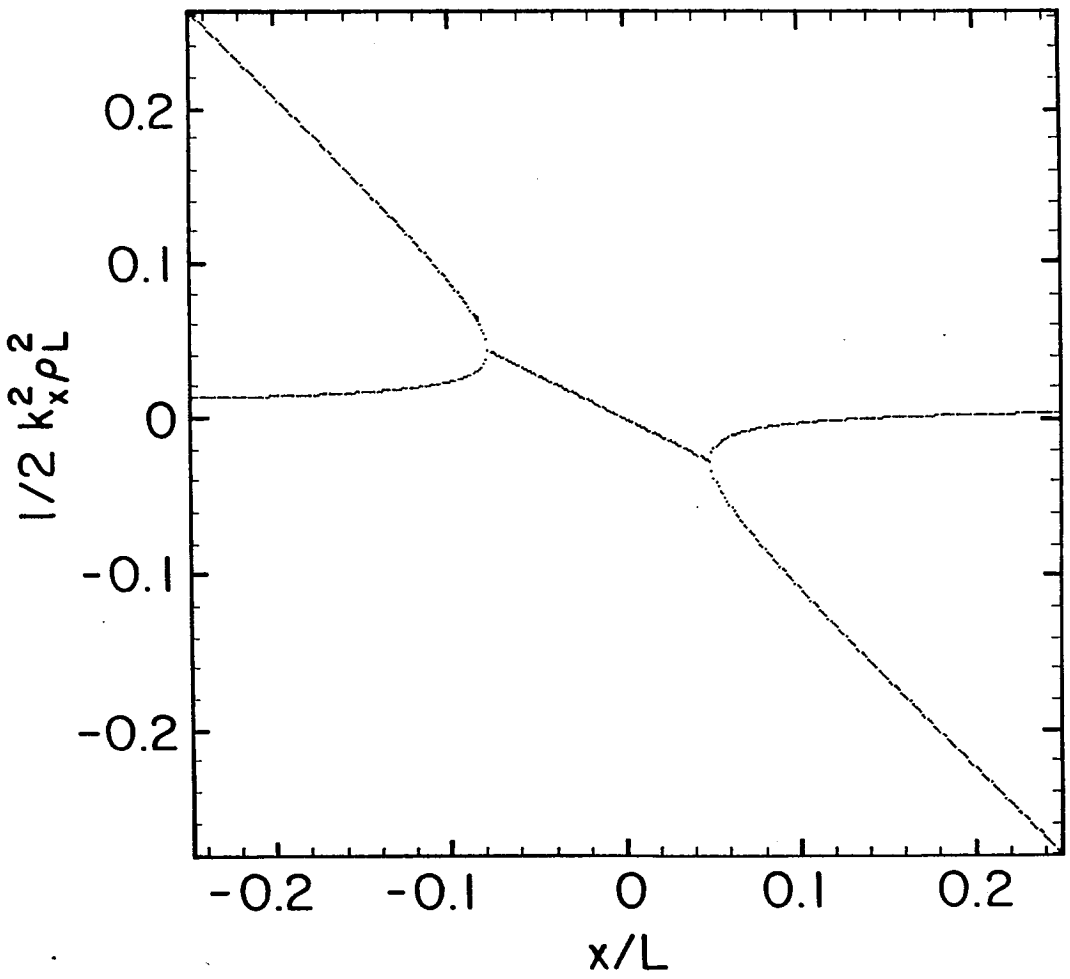


Fig. 2

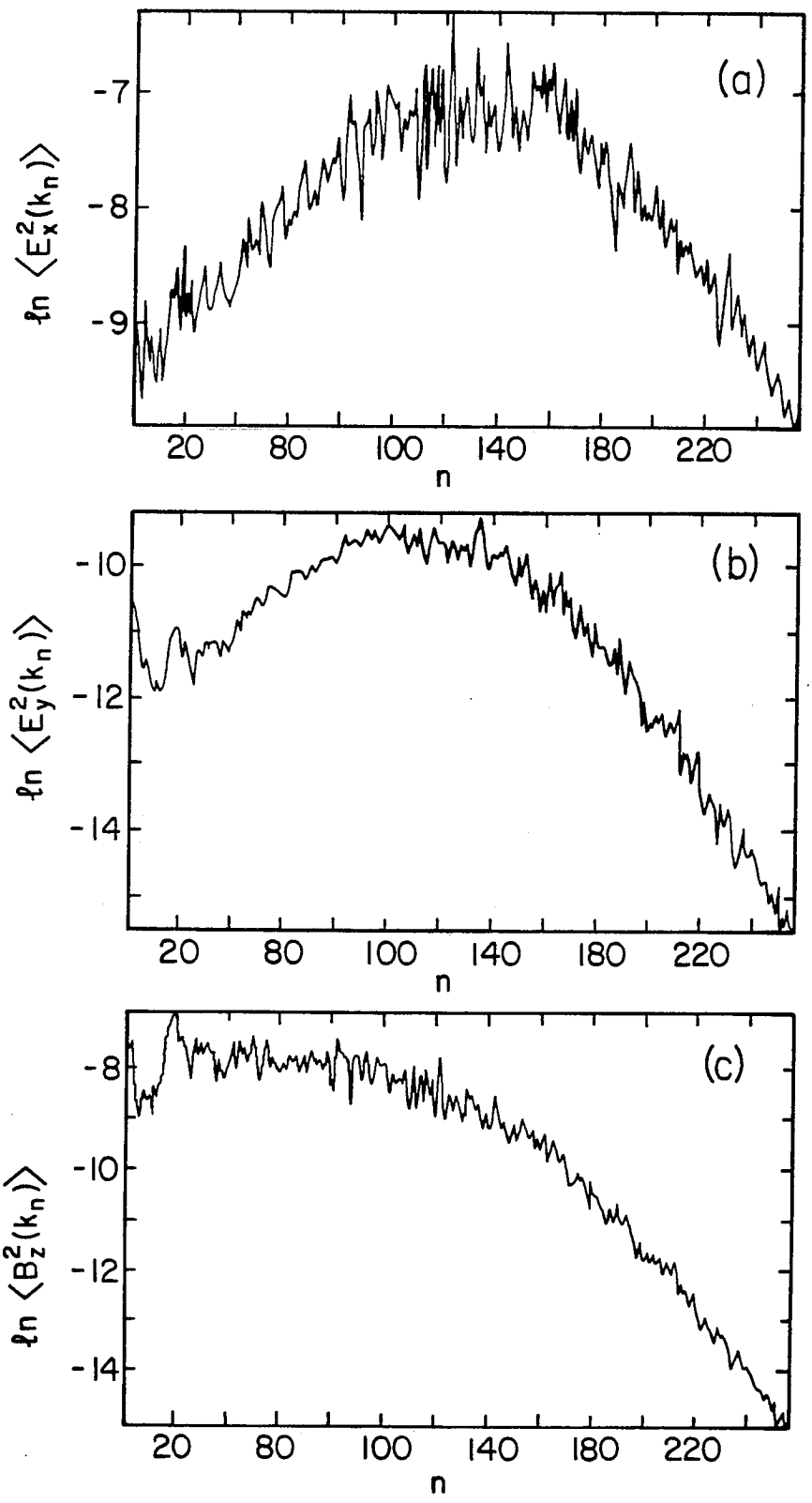
(a)
-7
-8
-9
ln ⟨E_x^2(k_n)⟩
20
80
100
140
180
220
n
(b)
-10
-12
-14
ln ⟨E_y^2(k_n)⟩
20
80
100
140
180
220
n
(c)
-8
-10
-12
-14
ln ⟨B_z^2(k_n)⟩
20
80
100
140
180
220
n

Fig. 3

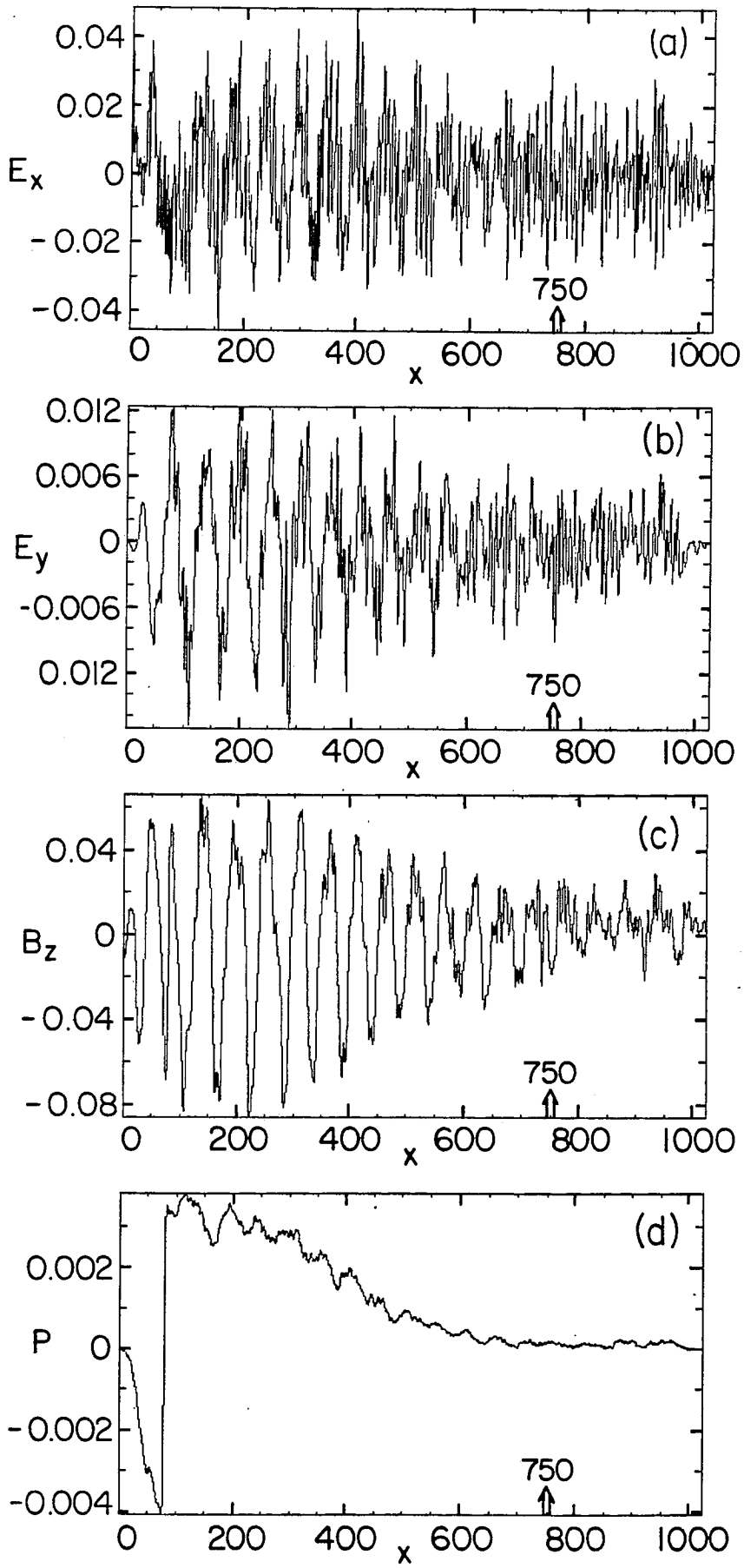
(a)
0.04
0.02
$E_x$ 0
-0.02
-0.04
750
0 200 400 600 800 1000
x
(b)
0.012
0.006
$E_y$ 0
-0.006
0.012
750
0 200 400 600 800 1000
x
(c)
0.04
$B_z$ 0
-0.04
-0.08
750
0 200 400 600 800 1000
x
(d)
0.002
P 0
-0.002
-0.004
750
0 200 400 600 800 1000
x

Fig. 4

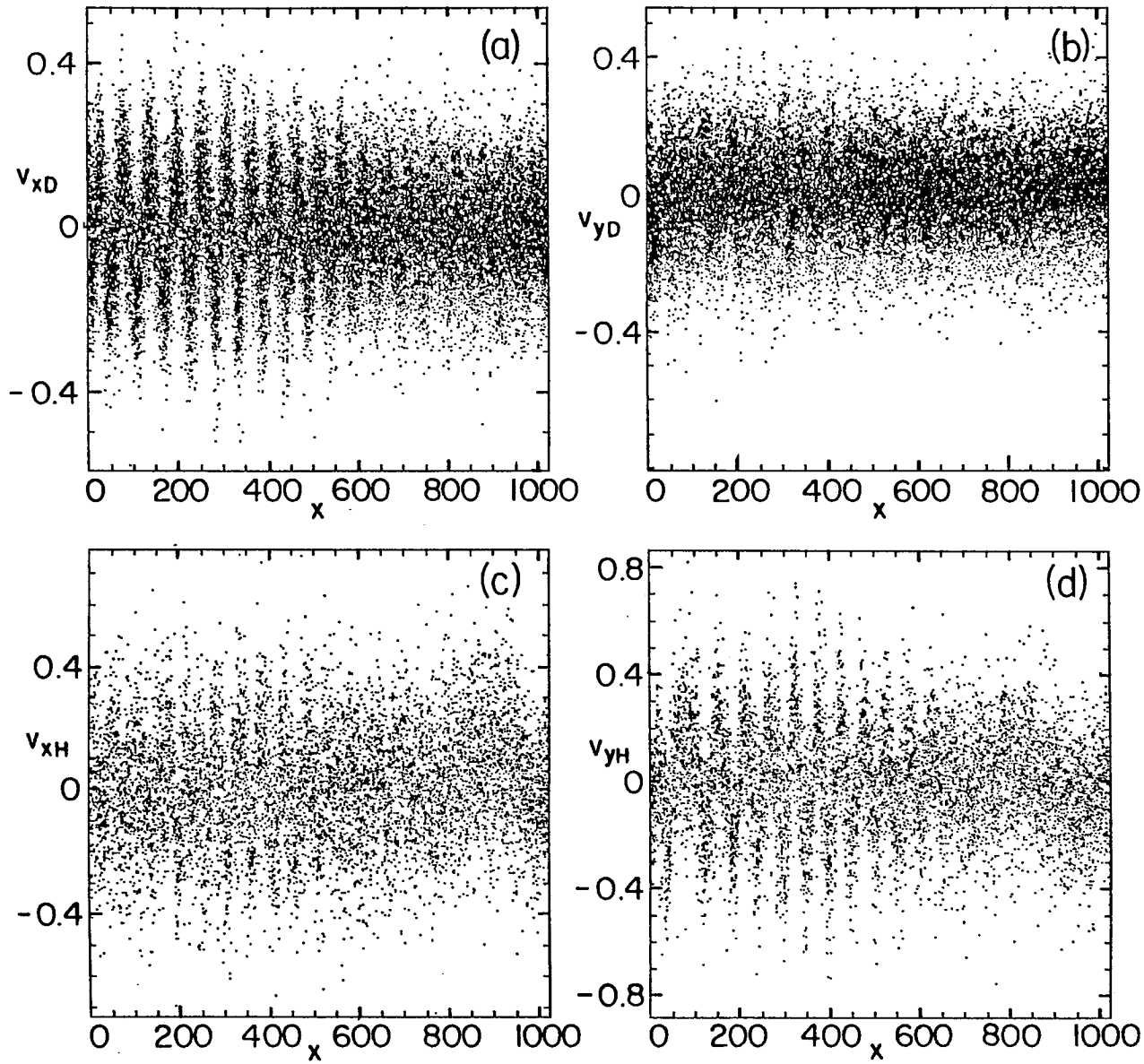


Fig. 5

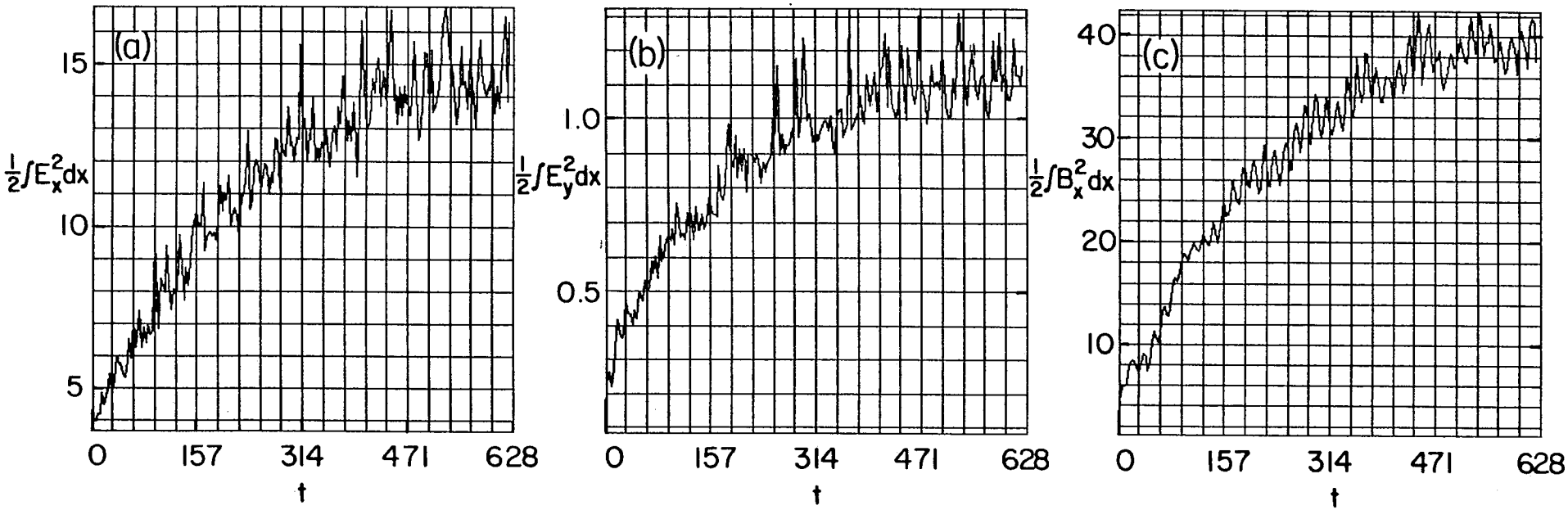
(a)
15
10
5
$\frac{1}{2}\int E_x^2 dx$
0
157
314
471
628
t
(b)
1.0
0.5
$\frac{1}{2}\int E_y^2 dx$
0
157
314
471
628
t
(c)
40
30
20
10
$\frac{1}{2}\int B_x^2 dx$
0
157
314
471
628
t

Fig. 6

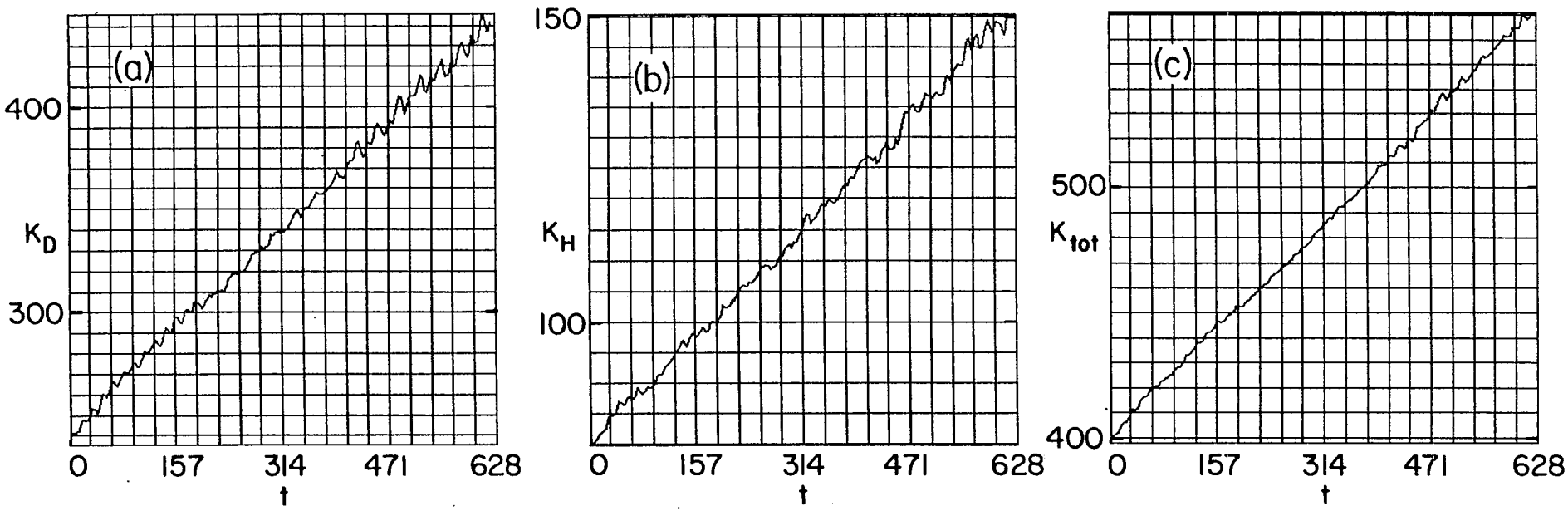
(a)
400
$K_D$
300
0
157
314
471
628
t
(b)
150
$K_H$
100
0
157
314
471
628
t
(c)
500
$K_{tot}$
400
0
157
314
471
628
t

Fig. 7

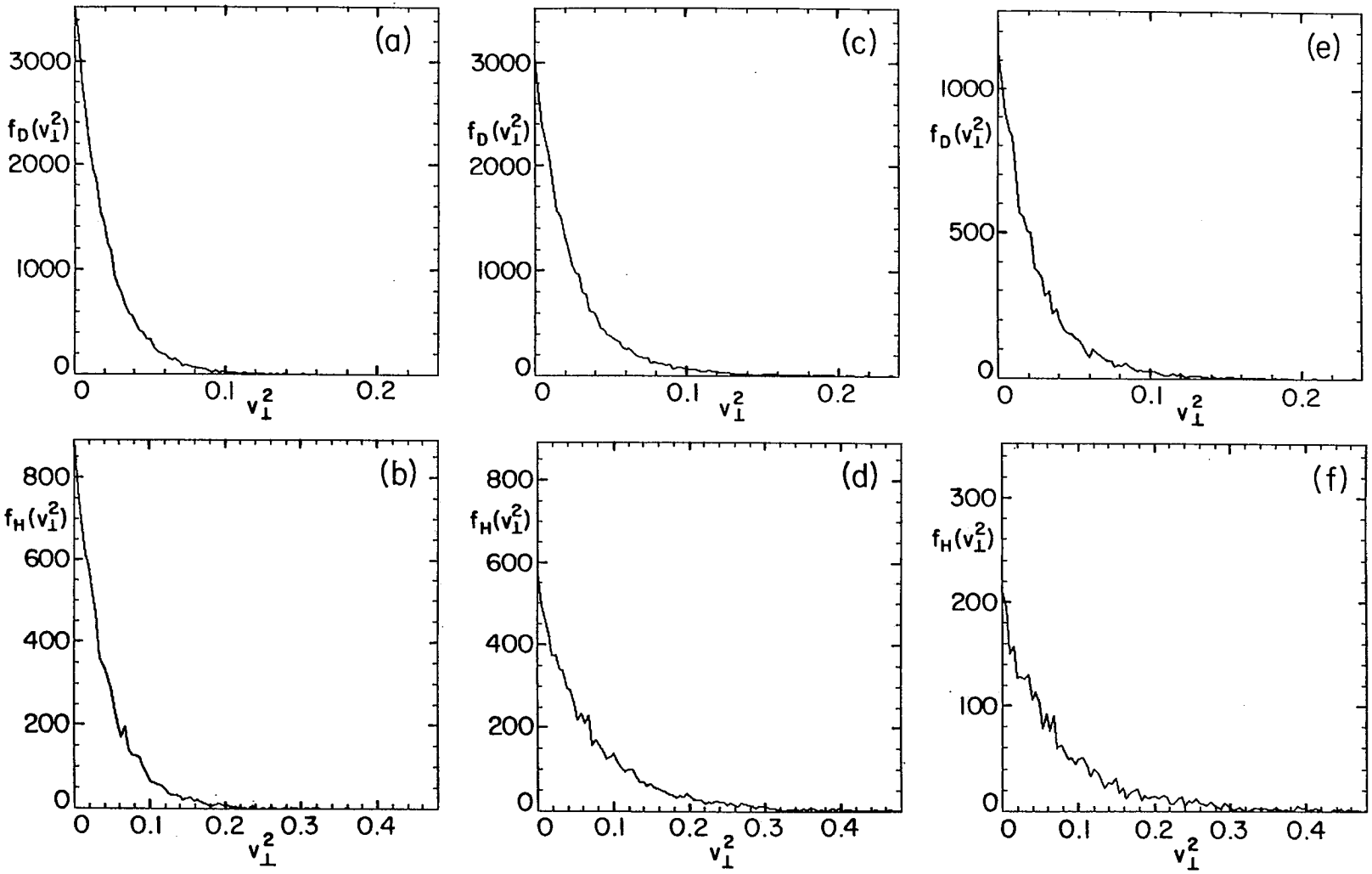
(a)
(b)
(c)
(d)
(e)
(f)
$f_D(v_\perp^2)$
$f_H(v_\perp^2)$
$v_\perp^2$
0
0.1
0.2
0.3
0.4
1000
2000
3000
500
200
400
600
800
100
300

Fig. 8

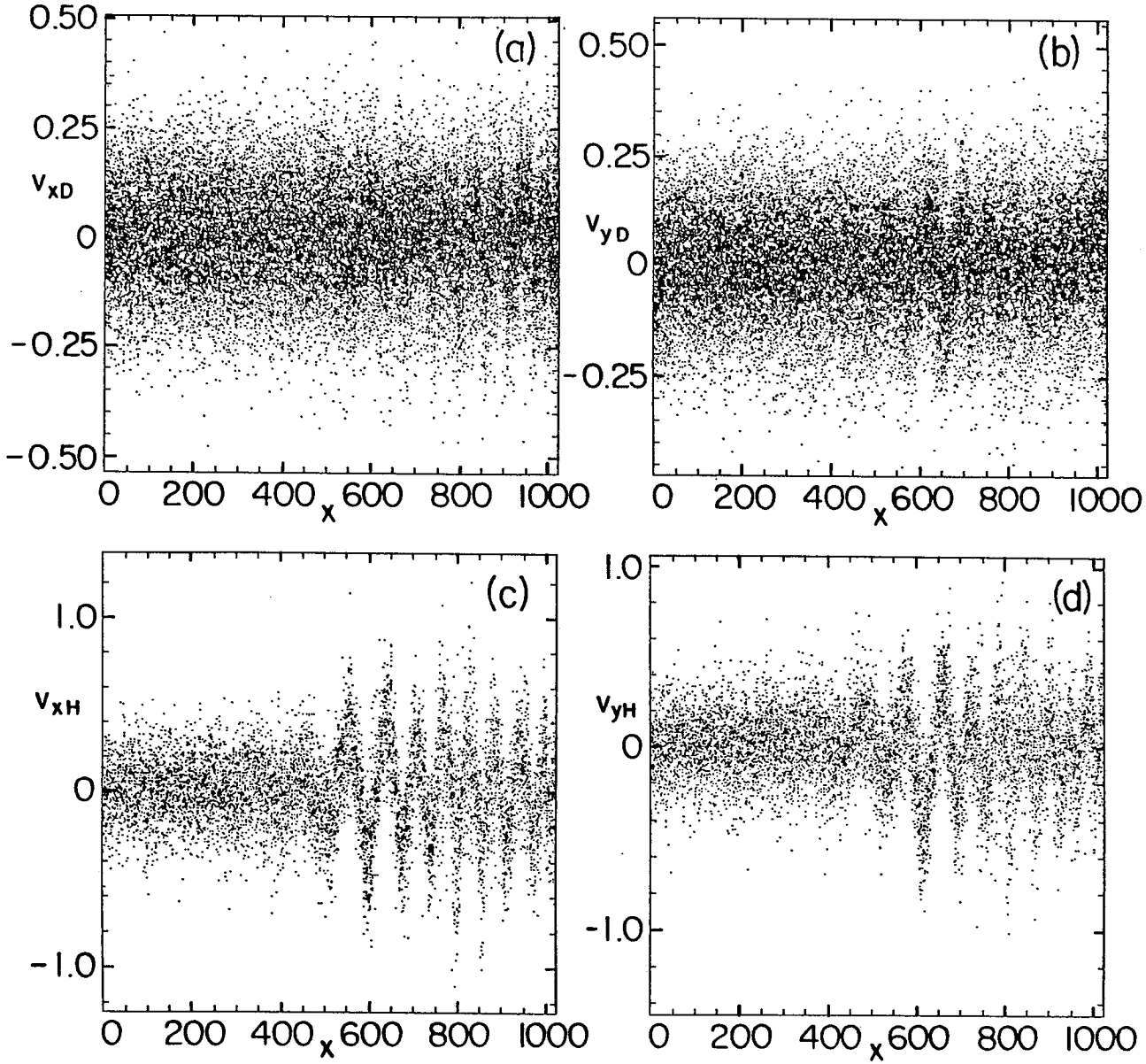
(a)
(b)
(c)
(d)
0.50
0.25
0
-0.25
-0.50
$V_{xD}$
$V_{yD}$
1.0
-1.0
$V_{xH}$
$V_{yH}$
0
200
400
600
800
1000
x

Fig. 9

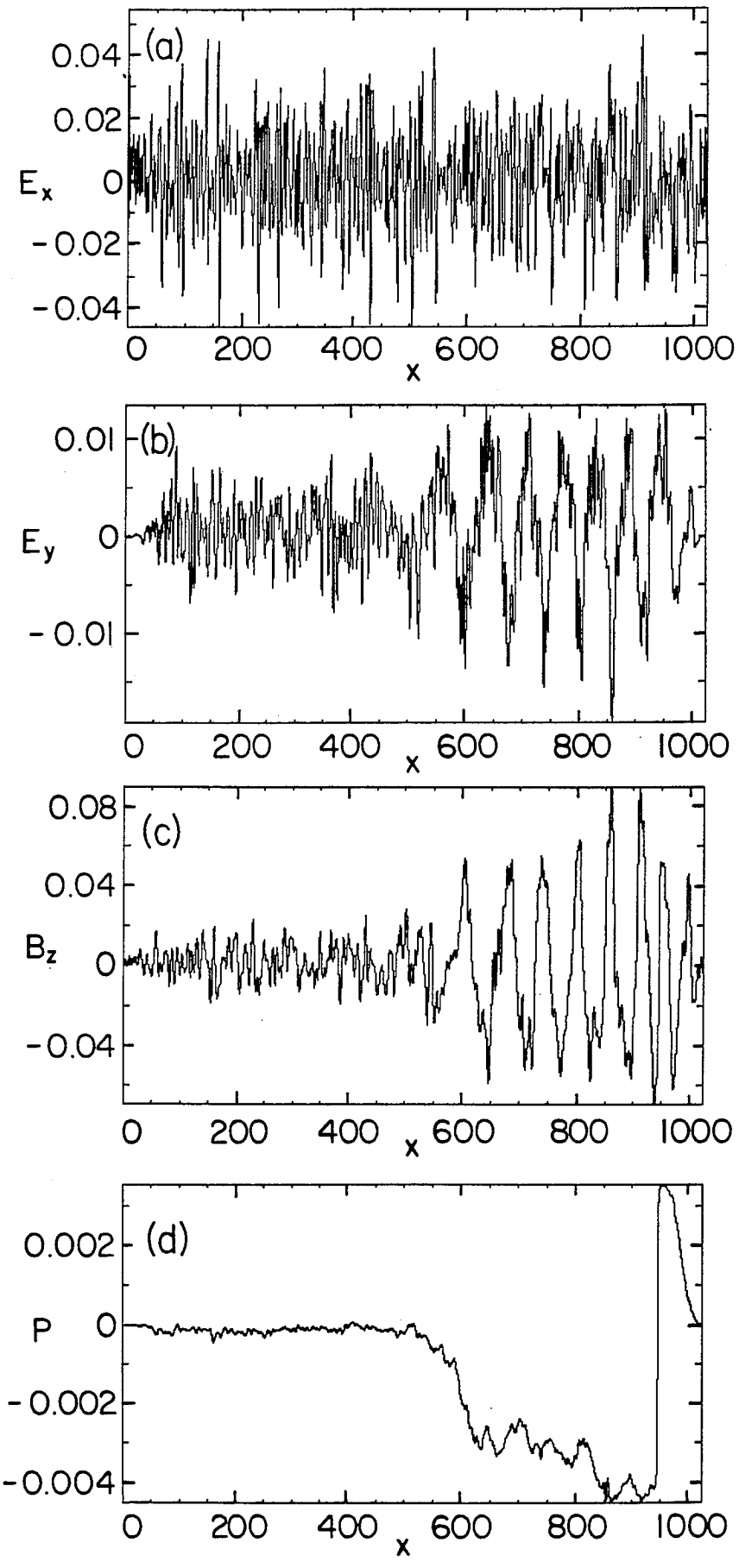
(a)
0.04
0.02
$E_x$ 0
-0.02
-0.04
0 200 400 600 800 1000
x
(b)
0.01
$E_y$ 0
-0.01
0 200 400 600 800 1000
x
(c)
0.08
0.04
$B_z$ 0
-0.04
0 200 400 600 800 1000
x
(d)
0.002
P 0
-0.002
-0.004
0 200 400 600 800 1000
x

Fig. 10

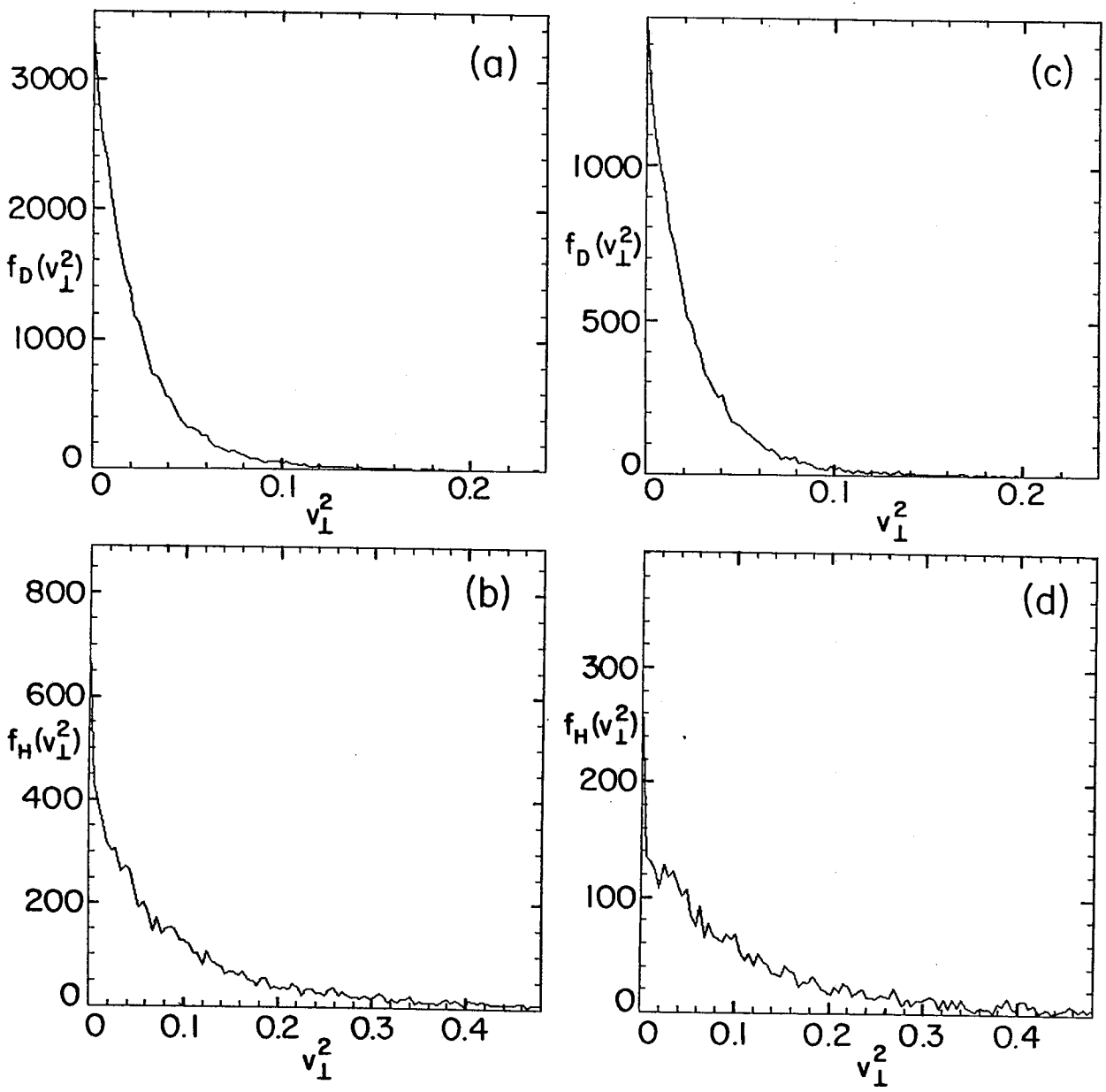
(a)
3000
2000
1000
0
$f_D(v_\perp^2)$
0
0.1
0.2
$v_\perp^2$
(c)
1000
500
0
$f_D(v_\perp^2)$
0
0.1
0.2
$v_\perp^2$
(b)
800
600
400
200
0
$f_H(v_\perp^2)$
0
0.1
0.2
0.3
0.4
$v_\perp^2$
(d)
300
200
100
0
$f_H(v_\perp^2)$
0
0.1
0.2
0.3
0.4
$v_\perp^2$

Fig. 11

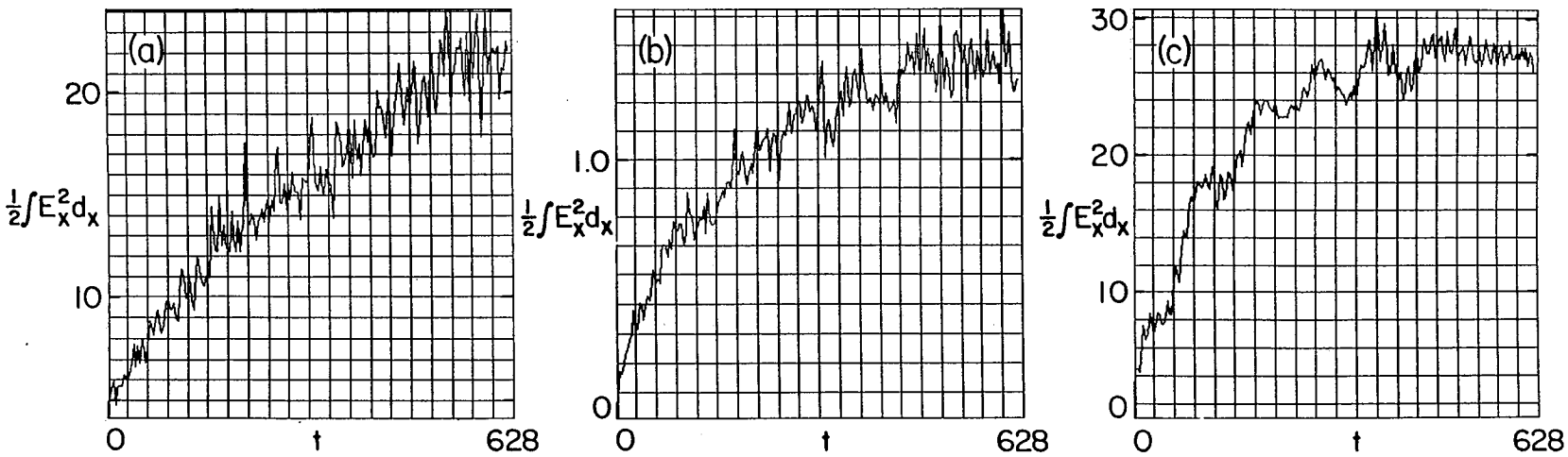
(a)
20
10
0
t
628
$\frac{1}{2}\int E_x^2 dx$
(b)
1.0
0
t
628
$\frac{1}{2}\int E_x^2 dx$
(c)
30
20
10
0
t
628
$\frac{1}{2}\int E_x^2 dx$

Fig. 12

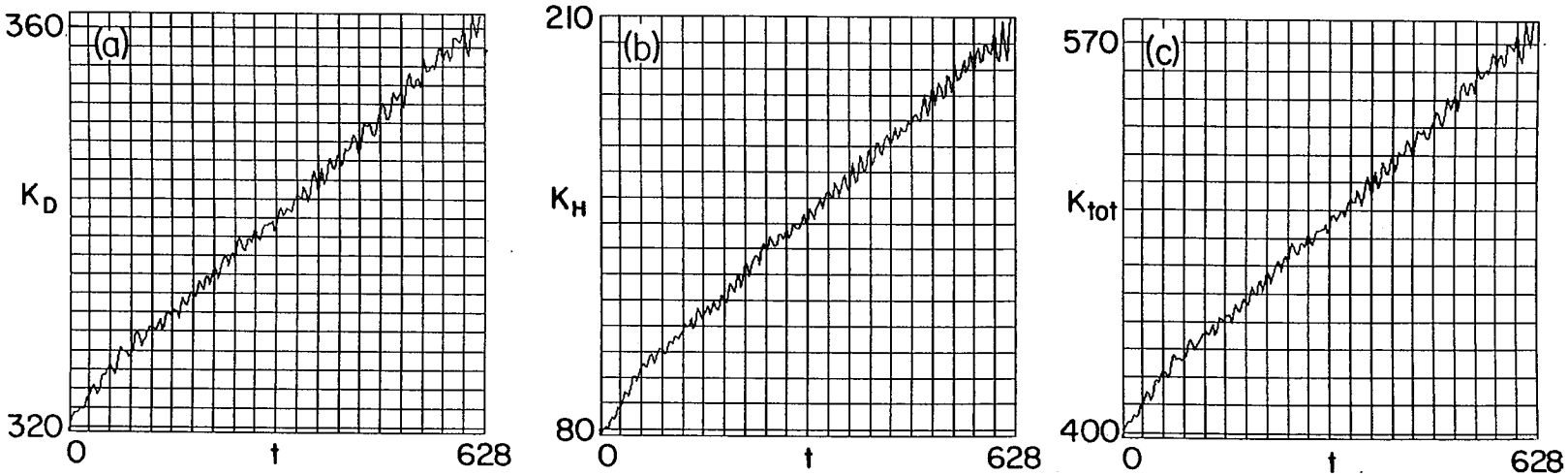


Fig. 13

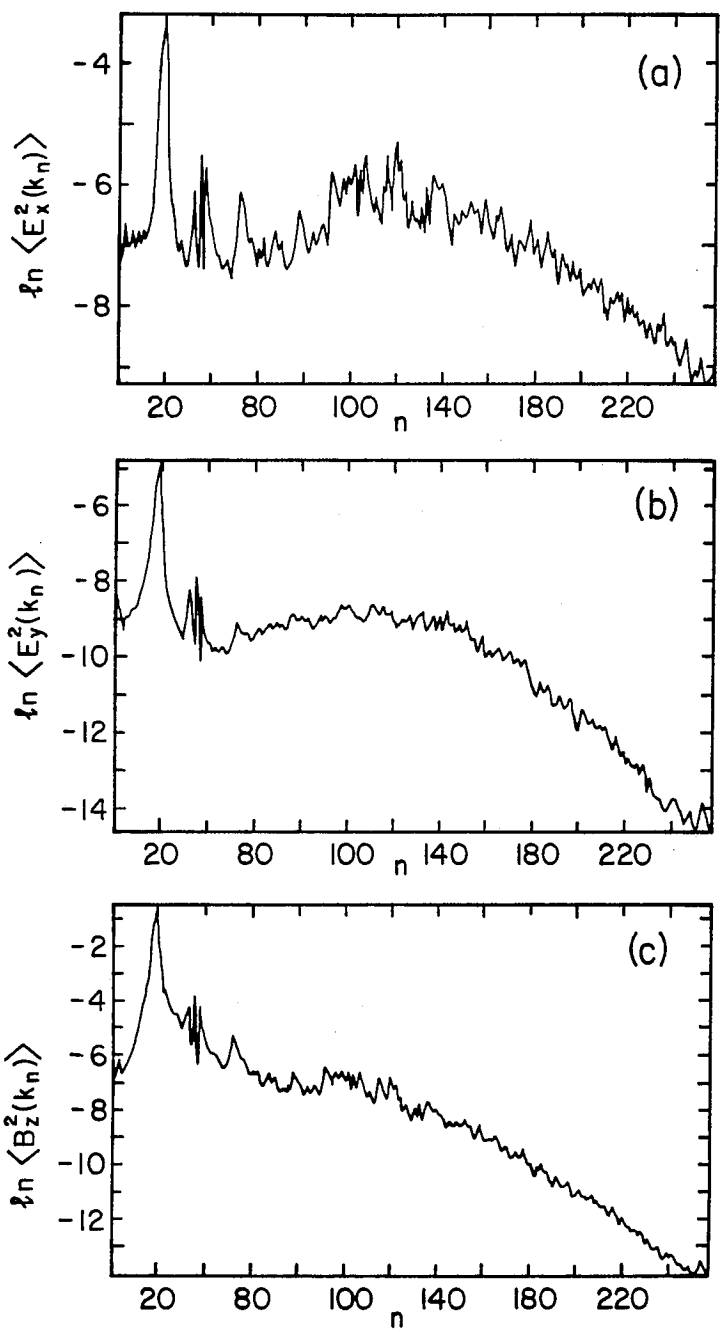
(a)
$\ell n \langle E_x^2(k_n) \rangle$
-4
-6
-8
20
80
100
n
140
180
220
(b)
$\ell n \langle E_y^2(k_n) \rangle$
-6
-8
-10
-12
-14
20
80
100
n
140
180
220
(c)
$\ell n \langle B_z^2(k_n) \rangle$
-2
-4
-6
-8
-10
-12
20
80
100
n
140
180
220

Fig. 14

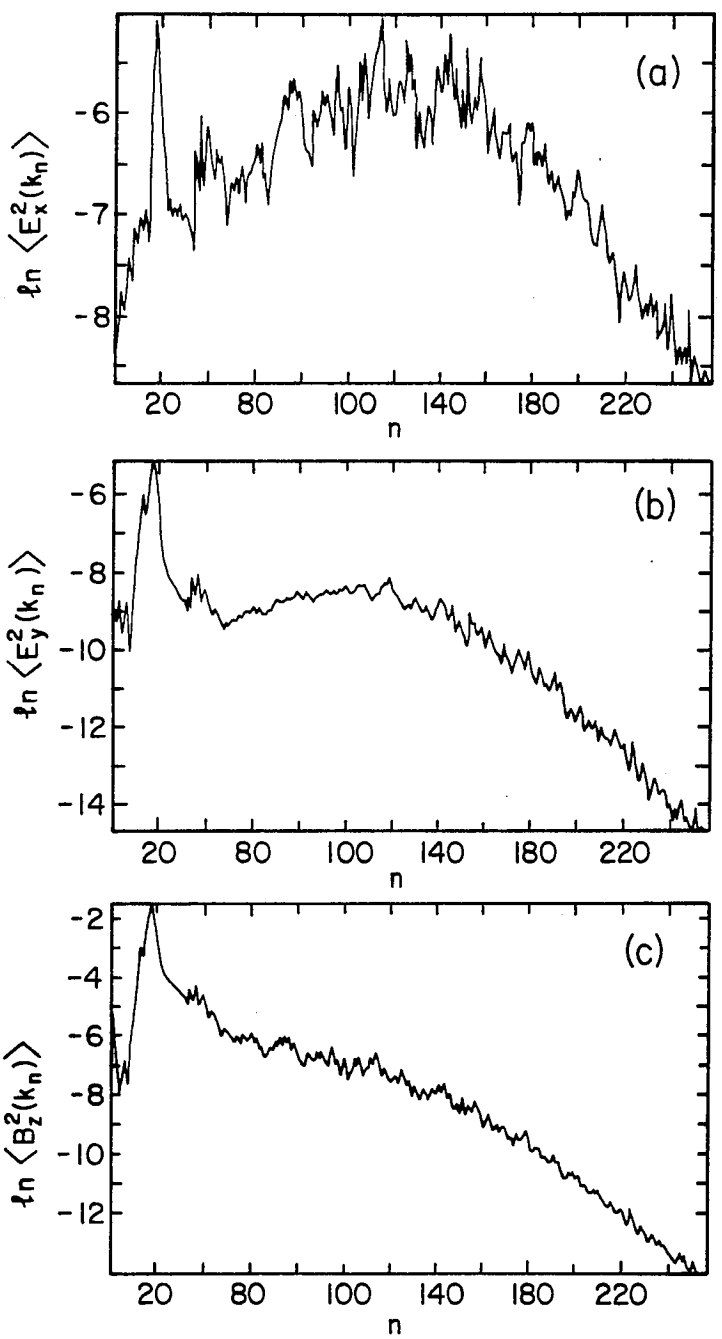
(a)
$\ell n \langle E_x^2(k_n) \rangle$
-6
-7
-8
20
80
100
140
180
220
n
(b)
$\ell n \langle E_y^2(k_n) \rangle$
-6
-8
-10
-12
-14
20
80
100
140
180
220
n
(c)
$\ell n \langle B_z^2(k_n) \rangle$
-2
-4
-6
-8
-10
-12
20
80
100
140
180
220
n

Fig. 15

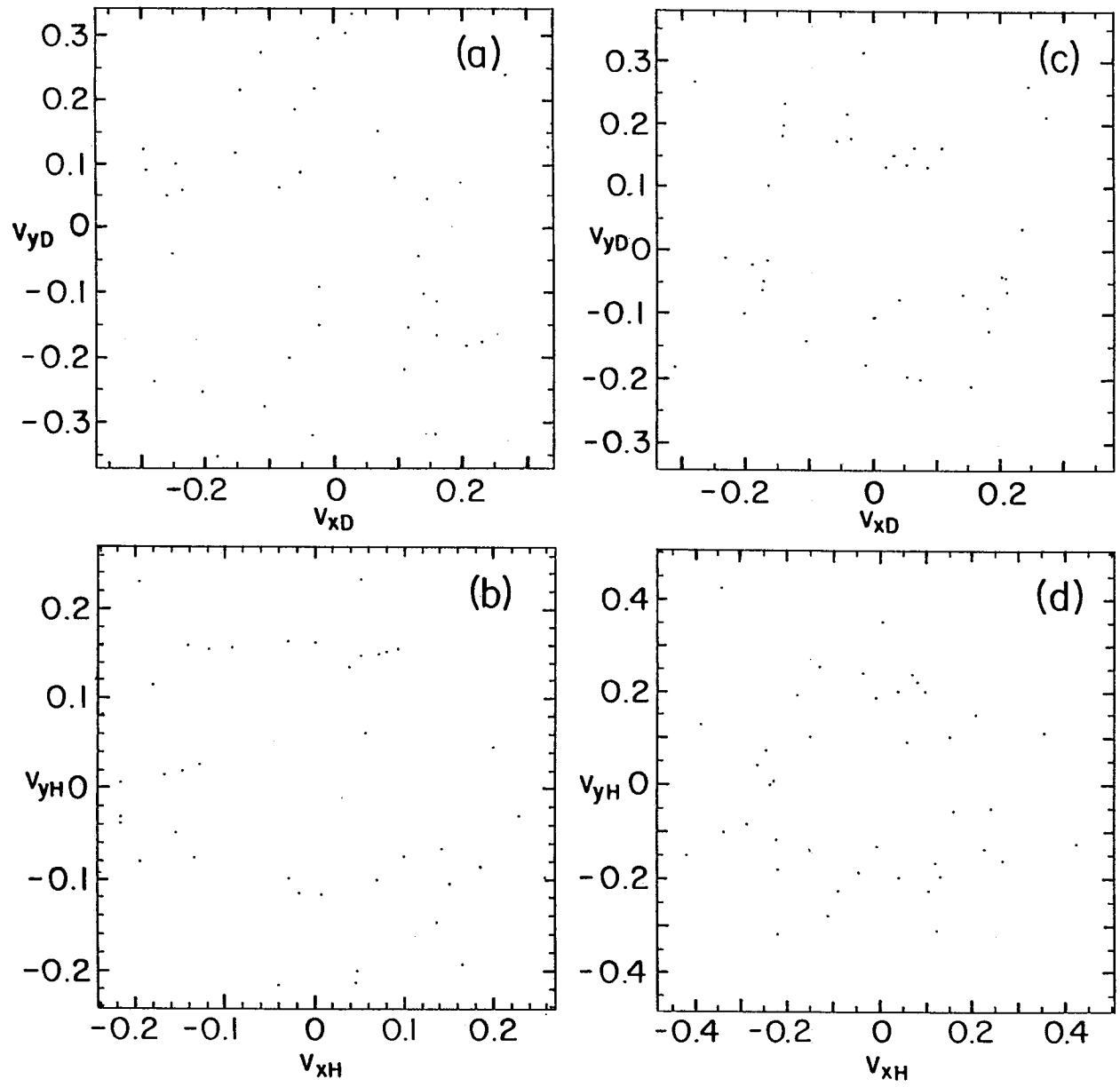


Fig. 16

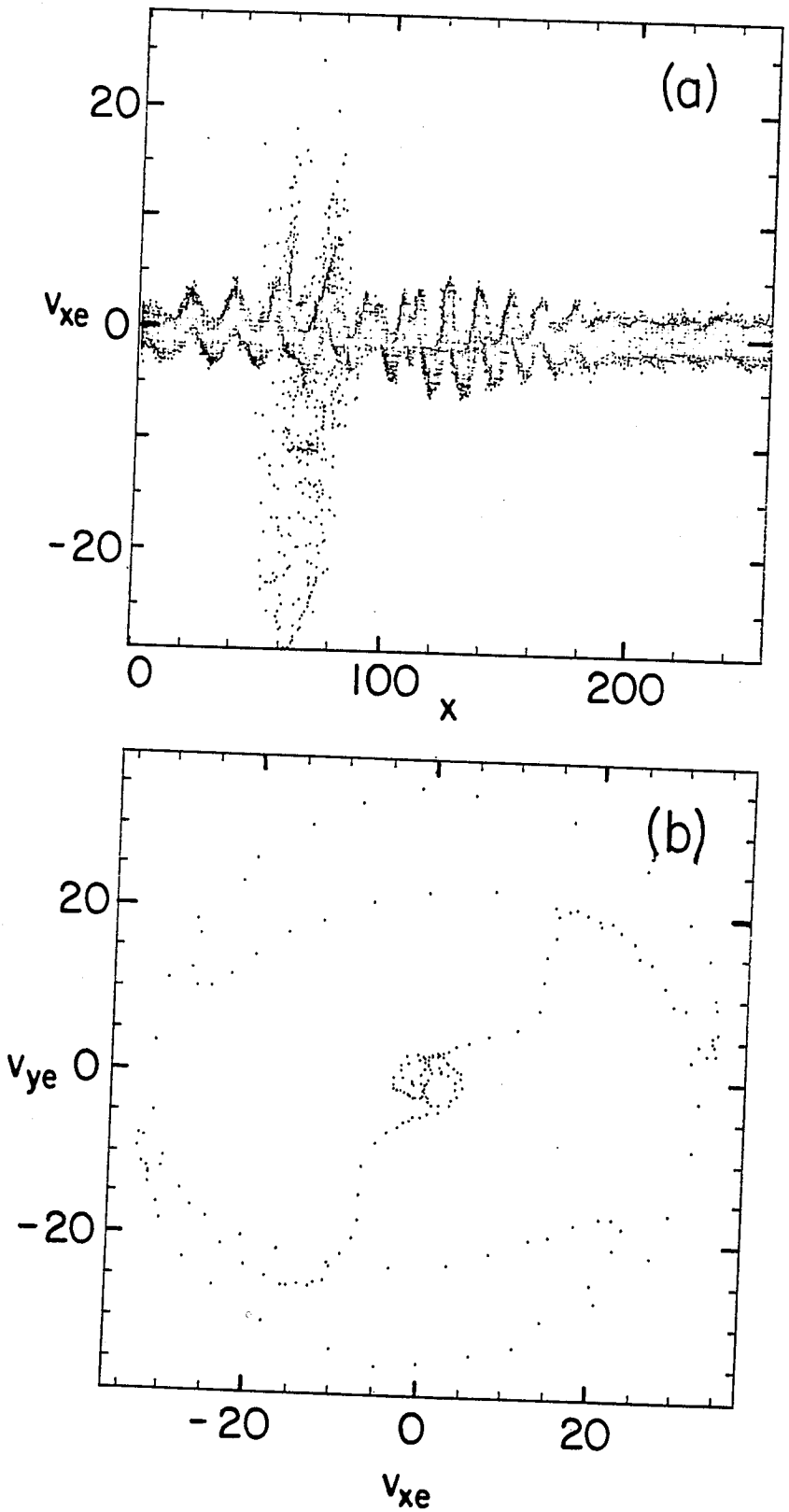


Fig. 17